

Mass loss and rotational CO emission from Asymptotic Giant Branch stars

F. Kemper^{1,2*}, R. Stark³, K. Justtanont⁴, A. de Koter¹, A.G.G.M. Tielens^{5,6}, L.B.F.M. Waters^{1,7},
J. Cami⁸, and C. Dijkstra¹

¹ Astronomical Institute “Anton Pannekoek”, University of Amsterdam, Kruislaan 403, 1098 SJ Amsterdam, The Netherlands

² UCLA, Division of Astronomy, 405 Hilgard Avenue, Los Angeles, CA 90095-1562, USA

³ Max-Planck-Institut für Radioastronomie, Auf dem Hügel 69, D-53121 Bonn, Germany

⁴ Stockholm Observatory, SCFAB, SE-106 91 Stockholm, Sweden

⁵ Kapteijn Institute, University of Groningen, P.O. Box 800, 9700 AV Groningen, The Netherlands

⁶ SRON Laboratory for Space Research, P.O. Box 800, 9700 AV Groningen, The Netherlands

⁷ Instituut voor Sterrenkunde, Katholieke Universiteit Leuven, Celestijnenlaan 200B, B-3001 Heverlee, Belgium

⁸ NASA Ames Research Center, Mail Stop 245-6, Moffett Field, CA 94035-1000, USA

Received / Accepted

Abstract. We present submillimeter observations of rotational transitions of carbon monoxide from $J = 2 \rightarrow 1$ up to $7 \rightarrow 6$ for a sample of Asymptotic Giant Branch stars and red supergiants. It is the first time that the high transitions $J = 6 \rightarrow 5$ and $7 \rightarrow 6$ are included in such a study. With line radiative transfer calculations, we aim to determine the mass-loss history of these stars by fitting the CO line intensities. We find that the observed line intensities of the high transitions, including the $J = 4 \rightarrow 3$ transition, are significantly lower than the predicted values. We conclude that the physical structure of the outflow of Asymptotic Giant Branch stars is more complex than previously thought. In order to understand the observed line intensities and profiles, a physical structure with a variable mass-loss rate and/or a gradient in stochastic gas velocity is required. A case study of the AGB star WX Psc is performed. We find that the CO line strengths may be explained by variations in mass-loss on time scales similar to those observed in the separated arc-like structures observed around post-AGB stars. In addition, a gradient in the stochastic velocity may play a role. Until this has been sorted out fully, any mass loss determinations based upon single CO lines will remain suspect.

1. Introduction

Low and intermediate mass stars ($1 < M < 8 M_{\odot}$) end their life on the red giant branch and asymptotic giant branch (AGB; see Habing 1996, and references herein). During the AGB phase, the stars have very extended tenuous atmospheres and shed almost their entire hydrogen-rich envelope through a dense and dusty stellar wind. In case of OH/IR stars, mass-loss rates can be so high that the dust shell completely obscures the central star, and the object is observable only at infrared wavelengths and through molecular line emission at radio wavelengths. The AGB phase is one of the few occasions in stellar evolution when time scales are not driven by nuclear (shell) burning but by surface mass loss. Helped by the low surface gravity and strong stellar pulsations, gas can move away from the star and will gradually cool. When the temperature drops below ~ 1400 K, dust formation occurs, and

a dust driven wind will develop. The mass-loss rates increase from $\dot{M} \approx 10^{-7}$ to a few times $10^{-5} M_{\odot} \text{ yr}^{-1}$, while the AGB star evolves from the Mira phase to an OH/IR star (van der Veen & Habing 1988). Recently, it has been suggested that higher mass-loss rates can be achieved for oxygen-rich AGB stars. Justtanont et al. (1996) find that OH 26.5+0.6 has undergone a recent increase in mass loss, leading to a current rate of $5.5 \cdot 10^{-4} M_{\odot} \text{ yr}^{-1}$, a result recently confirmed by Fong et al. (2002). Even higher mass-loss rates were found for another oxygen-rich AGB star, IRAS 16342–3814, for which the mass-loss rate may be as high as $\sim 10^{-3} M_{\odot} \text{ yr}^{-1}$ (Dijkstra et al. 2003). A similar rate of a few times $10^{-3} M_{\odot} \text{ yr}^{-1}$ is found for the carbon-rich evolved star AFGL 2688 (Skinner et al. 1997).

AGB stars are important contributors of dust to the interstellar medium (ISM); it is estimated that a substantial fraction of the interstellar dust is produced by oxygen-rich AGB stars (e.g. Gehrz 1989). In the outflow of evolved stars with an oxygen-rich chemistry the dust composition is dominated by silicates, both amorphous and crystalline

Send offprint requests to: F. Kemper (kemper@astro.ucla.edu)

* SIRTf Fellow

(e.g. Sylvester et al. 1999; Molster et al. 2002). The appearance of crystalline silicate features in the far-infrared spectra of AGB stars seems to be correlated with a high optical depth in the amorphous silicate resonance at 9.7 μm and hence a high mass-loss rate (Waters et al. 1996; Cami et al. 1998; Sylvester et al. 1999). This could be interpreted as evidence that a certain threshold value for the density is required to form crystalline silicates. However, Kemper et al. (2001) showed that observational selection effects may play an important role in detecting crystalline silicates in AGB stars with low mass-loss rates. Therefore, the relation between mass-loss rate and crystallinity remains unclear at present.

In order to further study the correlation between the wind density and the dust composition, reliable mass-loss rates should be determined. Mass-loss rates of AGB stars can be obtained from the thermal emission from dust, predominantly coming from the warm inner regions (e.g. Bedijn 1987). They can also be inferred from observations of molecular transitions, in particular from CO (e.g. Knapp & Morris 1985). A catalogue compiled by Loup et al. (1993) lists observations of the CO $J = 1 \rightarrow 0$ and $J = 2 \rightarrow 1$ transitions of both O-rich and C-rich AGB stars. (Hereafter we will use for these rotational transitions the notation CO(1–0) etc.) The mass-loss rates of a large number of objects from the catalogue are derived. However, the derived mass-loss rates seem to be underestimated for OH/IR stars, compared to the dust mass loss. Heske et al. (1990) have studied the correlation between IRAS colours and mass-loss rates derived from CO(2–1) and CO(1–0) observations. In the case of very massive dust shells, they find that the intensity of the CO(1–0) transition is too low compared to the CO(2–1) transition, which they suspect to be due to a mass-loss rate increase over time. This then hints towards a superwind phase, which is generally believed to be important in the evolution of a Mira towards an OH/IR star (e.g. Iben Jr. & Renzini 1983, and references herein). The superwind model was initially introduced to explain the amount of mass seen in planetary nebulae assuming that Miras are the progenitors of these nebulae (Renzini 1981). Miras are believed to evolve into OH/IR stars when they suddenly increase their mass-loss rate with a factor of ~ 100 .

As the inner regions are warmer they are better probed by higher rotational transitions. Thus a sudden density jump should be detectable in the CO lines. Model calculations by Justtanont et al. (1996) have demonstrated this effect for OH 26.5+0.6, using observations of rotational transitions up to CO(4–3). Unfortunately this transition is not sufficiently high to firmly establish the recent onset of a superwind, as its excitation temperature is only 55 K. Nevertheless, Justtanont et al. (1996) found that the peak intensities of these lines were significantly higher than what could be expected based on the extrapolation of the observed line strength of the CO(2–1) transition and the upper limit obtained for the CO(1–0) transition, assuming a constant mass-loss rate. Similar results are

Table 1. Technical details of the JCMT heterodyne receivers. The columns list the used receivers, the frequency windows at which they operate, the observable CO rotational transition, the beam efficiency η_{mb} and the half power beam width (HPBW).

receiver	Frequency (GHz)	CO transition	η_{mb}	HPBW
A3	215–275	CO(2–1)	0.69	19.7''
B3	315–373	CO(3–2)	0.63	13.2''
W/C	430–510	CO(4–3)	0.52	10.8''
W/D	630–710	CO(6–5)	0.30	8.0''
E	790–840	CO(7–6)	0.24	6.0''

reported for other AGB stars (e.g. Groenewegen 1994b; Delfosse et al. 1997).

The work presented here aims to determine the mass-loss history of a number of oxygen-rich AGB stars with an intermediate or high optical depth in the near- and mid-infrared. For the first time, observations of rotational transitions up to CO (7–6) have been obtained ($T_{\text{ex}} = 155$ K) which probe the more recent mass-loss phases. In Sect. 2 we describe the observations and data analysis. Sect. 3 describes the model. Our results are discussed in Sect. 4. Concluding remarks and an outlook to future work is presented in Sect. 5.

2. Observations and data reduction

2.1. Instrumental set-up

Observations of the $^{12}\text{CO}(2-1)$, (3–2), (4–3), (6–5) and (7–6) rotational transitions in the outflow of evolved stars were obtained during several observing periods between April 2000 and September 2002 using the *James Clerk Maxwell Telescope* (JCMT) on Mauna Kea, Hawaii. For this purpose, all five different heterodyne receivers available at the JCMT were used, including the new MPIfR/SRON E-band receiver which operates in the 790–840 GHz frequency range. A description of this new receiver is given in Sect. 2.2. The technical details and beam properties of the JCMT set up with the appropriate heterodyne receivers are summarized in Table 1. Observations with the B3- and W-receivers were performed in double sideband (DSB) and dual polarization mode. The DSB mode was also used for the observations with the MPIfR/SRON E-band receiver. The bandwidth configuration of the receiver, and hence the spectral resolution was determined by the expected line width of the CO lines. We used bandwidths of at least twice the expected line width to have a sufficiently broad region for baseline subtraction. Estimates for the line width – which is determined by the outflow velocity – were based on published values of line widths of the CO(1–0) transition (e.g. Loup et al. 1993, and references herein).

We used the beam-switching technique to eliminate the background. The secondary mirror was chopped in

azimuthal direction over an angle of $120''$. Over these small angles the noise from the sky is assumed to be constant. In case of extended sources we used a beam-switch of $180''$.

2.2. The MPIfR/SRON 800 GHz receiver

The observations of the CO(7–6) line were made with the MPIfR/SRON 800 GHz receiver in October 2001. This PI system is in operation at the JCMT Cassegrain focus cabin since spring 2000. The receiver consists of a single-channel fixed-tuned waveguide mixer with a diagonal horn. The mixer consists of a Nb SIS junction with NbTiN and Al wiring layers fabricated at the University of Groningen, The Netherlands. Details on the fabrication of similar devices can be found in Jackson et al. (2000). Measured receiver temperatures at the cryostat window are $T_{\text{Rx}} \simeq 550$ K DSB. The receiver has an intermediate frequency of 2.5 – 4 GHz. System temperatures including atmospheric losses varied between 6000–14000 K (SSB) at the time of the observations. The beam shape and efficiency have been determined through observations of Mars and yield a deconvolved half power beam width (HPBW) of $6''$ and a main beam efficiency η_{mb} of 24%.

2.3. Observations and data reduction

Our sample of evolved stars is given in Table A.1, which also indicates the distances towards the programme stars. The sample includes AGB stars and red supergiants. In Table A.2 an overview of the observed transitions is given, including cumulative integration times and the observing date. The data were obtained over a long period from April 2000 until September 2002 in flexible observing mode, and are part of a larger ongoing programme. During the observations, spectra of CO spectral standards used at the JCMT were also obtained. If necessary, a multiplication factor was applied to the observations of our sample stars, to correct for variations in the atmospheric conditions. These factors are listed in Col. 4 of Table A.2 and are based on measured standard spectra. Reliable standards are only available for the transitions observed with the A3-, B3- and W/C-receivers, for which the flux calibration accuracy is around 10%. For the W/D- and MPIfR/SRON E-band reliable standards for our lines of interest are lacking. Therefore we estimate that the absolute flux calibration in these bands has an accuracy of 30%.

Table 1 lists the beam efficiencies η_{mb} for all receivers. The main beam temperatures were calculated according to $T_{\text{mb}} = T_{\text{A}}^*/\eta_{\text{mb}}$, where T_{A}^* is the measured antenna temperature. These main beam temperatures can directly be compared to observations from other telescopes.

The reduced data is presented in Table A.3. A linear baseline has been subtracted from the raw data, and the spectrum has been rebinned to improve the signal-to-noise ratio. We aimed to cover the line profile with at least ~ 80 bins, which limits the rebinning factor. The bin sizes after rebinning and the corresponding r.m.s. values are listed in

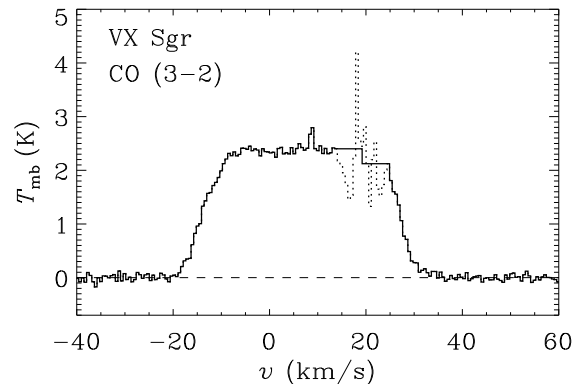


Fig. 1. Correction of the profile of the CO(3–2) transition of VX Sgr. The dotted line represents the observation in which the interstellar contribution is clearly visible. Ignoring the interstellar contribution results in the solid line, which is used to obtain the integrated intensity.

Cols. 4 and 5 of Table A.3. Emission lines were detected in almost all observations, except for α Sco CO(3–2) and OH 104.9+2.4 CO(6–5) and (7–6), for which we only obtained upper limits on the main beam temperatures. The line profiles of all transitions are shown in Figs. A.1–A.21. In some cases, interstellar lines are visible in the spectrum, for example in VX Sgr. To determine the integrated intensities we have cut the interstellar lines out of the spectrum, and interpolated both parts of the spectrum, as is demonstrated in Fig. 1. The resulting profile was integrated to obtain I , which is the integrated intensity in K km s^{-1} . The system velocity V_{LSR} and the terminal expansion velocity v_{∞} are estimated directly from the line profile. The lines show a wide variety of shapes. There are parabolic line profiles, like those of WX Psc (Fig. A.1), IRC+50137 (Fig. A.5), AFGL 5379 (Fig. A.10), CRL 2199 (Fig. A.12) and OH 104.9+2.4 (Fig. A.21). These parabolic line profiles indicate that the lines are optically thick (Morris 1980). On the other hand, many objects show signs the double-horned profiles indicative of an optically thin molecular layer. The most illustrative example is VY CMa, in which the CO(2–1) and CO(3–2) transitions clearly show a double-peaked profile, although the peak around the central velocity indicates a more complex outflow structure (Fig. A.9). In addition, some flat-topped profiles are observed, most notably those of VX Sgr (Fig. A.11). These flat-topped line profiles are considered to be characteristic of molecular layers which have $\tau \sim 1$ at these frequencies (Morris 1980).

Justtanont et al. (1996) have observed OH 26.5+0.6 with the JCMT as well and report that they find line intensities $I = 25.8$ and 36.0 K km s^{-1} for the CO(3–2) and (4–3) transition respectively. In addition they have scaled IRAM observations of the CO(2–1) to a 15m dish, to mimic the JCMT. The intensity of this line turned out to be 7.8 K km s^{-1} . Their results agree well with our results in case of the CO(2–1) and (3–2) transition, but

they have observed an intensity of a factor of ~ 2 higher for the CO(4–3) transition. The origin of the discrepancy with our results is unknown.

3. Physical conditions in the outflow: a model

The observed line profiles provide information on the physical structure of the outflow of these AGB stars, as the spectral resolution at the observed frequencies is sufficiently high to resolve the velocity structure. The terminal expansion velocity v_∞ can be derived directly from the width of the line profile (Table A.3). The model we use to analyze the CO data is based on a study by Schönberg (1988) and was previously used by Justtanont et al. (1994). The interpretation of our observations using this model is discussed in Sect. 4.

3.1. Description of the model

The code consists of two parts: The first part solves the radiation transfer equation in the co-moving frame (Mihalas et al. 1975), computes the level populations (in full non-LTE) and iterates until level populations and radiation field are consistent. For solving the level populations, a Newton-Raphson method is used (Schönberg & Hempe 1986). The calculations take into account (de-)excitation through collisions, of which the rate is defined by the thermal velocity distribution, calculated from the local temperature, as well as (de-)excitation induced by a local radiation field and spontaneous de-excitation. The code treats pure rotational transitions in the ground and first vibrational levels, which are connected through these collisional and radiative transitions. The model can calculate the populations of as many as 50 levels at once, and is also applicable to molecules other than CO. The non-LTE rate equations to determine the level populations are described by

$$n_i \sum_{j \neq i} (A_{ij} + C_{ij} + B_{ij} \bar{J}_{ij}) - \sum_{j \neq i} n_j (A_{ji} + C_{ji} + B_{ji} \bar{J}_{ij}) = 0 \quad (1)$$

A change from level i to level j can be induced by collisional transitions (with the collisional rate C_{ij}) and radiative transitions, including spontaneous emission (A_{ij} , where $A_{ij} = 0$ for $i < j$) and stimulated emission and absorption ($B_{ij} \bar{J}_{ij}$). The collisional transition rates C_{ij} are taken from laboratory measurements and potentials calculations (Flower & Launay 1985) and are extended up to $J = 30$.

The line profile integrated mean intensity \bar{J}_{ij} consists of two components:

i) The *continuum* radiation, originating from dust locally present. This radiation field can be switched off, by assuming there is no dust present in the considered part of the outflow.

ii) Line radiation originating from a local region. The size of this region is defined by a velocity which Schönberg (1988) and also Justtanont et al. (1994) have referred to as *stochastic* velocity v_{sto} . The nature of this *stochastic* velocity is not specified, but physically should consist of a thermal component v_{therm} and a turbulent component v_{turb} , given by

$$v_{\text{sto}} = \sqrt{(v_{\text{therm}})^2 + (v_{\text{turb}})^2} \quad (2)$$

In the outflow, the stochastic velocity is assumed to be constant and in almost all cases dominated by turbulence. The effect of the stochastic velocity is Doppler broadening of the lines, which is taken into account in the radiative transfer.

In the second part of the code, the calculated level populations are used as input to determine the observable line profiles by ray-tracing. Again the *stochastic* velocity is used, this time to determine the width of the interaction region along the line-of-sight to the observer. Integration over the full beam, for which the telescope parameters are required, yields the emergent line profile.

3.2. Free parameters

The model has a number of free parameters (see Table 2). In this section we will discuss the various parameters and their relevance for the model calculations.

3.2.1. Density profile

The density profile $\rho(r)$ of the outflow determines the collision probabilities and optical depths required to solve Eqs. (1) and to calculate the line profiles. The density profiles follows from the equation of mass continuity

$$\rho(r) = \frac{\dot{M}}{4\pi r^2 v_{\text{exp}}(r)} \quad (3)$$

where the expansion (or outflow) velocity profile used in the model is defined by

$$v_{\text{exp}}(r) = v_\infty \left(1 - \frac{b}{r} \right) \quad (4)$$

In this equation v_∞ represents the terminal velocity. Constant b is chosen such that the expansion velocity at the stellar surface is given by $v_{\text{exp}}(R_*) = 10^{-2} v_\infty$. The density structure is set by the following input parameters

i) The gas *mass-loss rate* \dot{M} determines the mass input at the inner radius of the circumstellar shell. Our model allows us to simulate the effect of a time-variable mass-loss rate introducing *one jump* in the mass-loss history at an arbitrary point in the outflow ($r_{\text{superwind}}$), where the density can increase or decrease with a specified factor. Except for this jump the mass-loss rate is constant, and therefore the density profile scales with the current mass-loss rate at $r < r_{\text{superwind}}$ and with the past mass-loss rate at $r > r_{\text{superwind}}$.

- ii) The density profile also scales with the outflow velocity profile given in Eq. (4), which is fixed by the *terminal velocity* v_∞ .
- iii) The *stellar radius* R_* determines the base of the wind. The density $\rho(R_*)$ at the inner radius follows from R_* , \dot{M} and $v_{\text{exp}}(R_*)$ using the equation of mass continuity (3).
- iv) The *outer radius* R_{out} denotes the extent of the outflow.

3.2.2. Temperature profile

The *temperature profile* $T(r)$ is another important parameter that influences the level populations in the circumstellar CO, by means of collisions. The temperature profile may be compiled self-consistently, i.e. based on calculations of realistic heating and cooling processes (e.g. Goldreich & Scoville 1976; Justtanont et al. 1994; Chen & Neufeld 1995; Zubko & Elitzur 2000). As a first order estimate we have used a power law of the form $T(r) \propto r^{-\alpha}$, where the index α depends on the mass-loss rate and is derived from the outer regions of the temperature profiles calculated by Justtanont et al. (1994).

3.2.3. Dust-to-gas ratio and dust properties

Unfortunately it is difficult to study the gas and dust mass-loss rate completely independent from each other, as continuum emission from dust may have an effect on the (de-)excitation rates, as described in Sect. 3.1. In particular, infrared photons at $4.6 \mu\text{m}$ pump CO molecules from the ground vibrational state $v = 0$ to the first vibrational level $v = 1$ (e.g. Morris 1980; Schönberg 1988). The molecules will eventually de-excite to the vibrational ground level, but not necessarily to the same rotational ground level. This causes a higher population of the higher CO rotational levels than which reflects the kinetic temperature of the gas and the line radiation field. As the source of the $4.6 \mu\text{m}$ radiation is predominantly thermal dust emission, the *dust-to-gas ratio* and the *dust opacity* are important input parameters. For simplicity, we assumed that there was no dust present in the outflows. For some of the calculations we did include dust to study the effect on the line strengths. In those cases we used a dust opacity corresponding to the mixture of solid state components derived for OH 127.8+0.0, a typical OH/IR star (Kemper et al. 2002). The same power-law temperature distribution as for the gas is used to calculate the thermal emission from the grains, although this is most likely not true.

3.2.4. Velocity field

The velocity field has already been mentioned as a constraint for the density structure, but it also plays an important role in the formation of line profiles. The outflow velocity profile (constrained by the *terminal velocity* v_∞

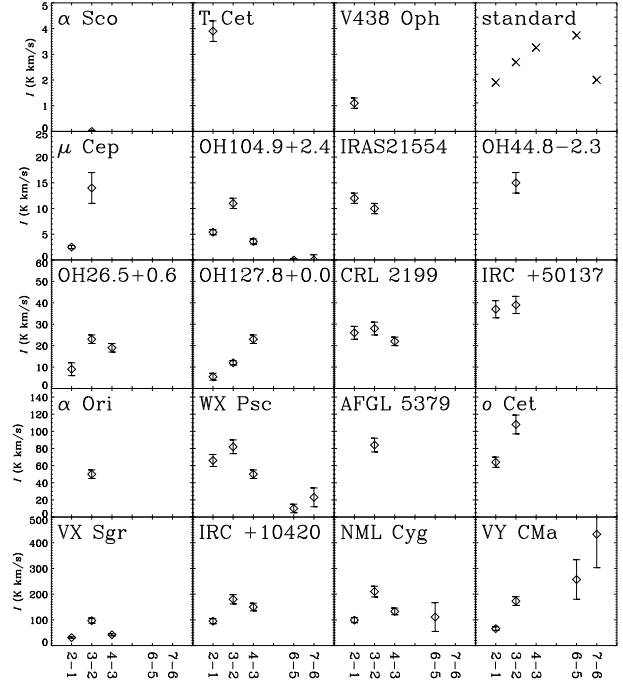


Fig. 2. Overview of integrated intensities for each line observed in our programme stars. The horizontal axis of each panel lists the rotational transitions observed, where the spacing between the tick marks is proportional to the difference in frequency. On the vertical axis the integrated intensity (K km s^{-1}) is given. The diamonds represent the measured values; in addition the error bars are shown (data from Table A.3). Note that only the line strengths of VY CMa increase with higher rotational transitions. For most of the other stars (except OH 127.8+0.0, IRC +50137 and IRAS 21554+6204) CO (3–2) is the brightest line. In the upper right corner the relative values for the standard model (see Table 2, Fig. 3) are presented for comparison (indicated with \times symbols).

and the velocity law given in Eq. (4)) and the *stochastic velocity* v_{sto} determine the location and extent of the interaction regions. As said before, the stochastic velocity is assumed to be constant throughout the dust shell.

3.2.5. Distance and telescope parameters

The resulting main beam temperatures depend on the *distance* towards the object. In addition, the telescope *beam size* is important to determine what part of the object falls inside the beam. In case the circumstellar shell is resolved, the *pointing displacement* (usually $0''$) should be known as well.

4. Analysis of the results

Here we will analyze the observations using the model described in Sect. 3. Fig. 2 shows the intensities integrated over line width of each observed line for all our sample

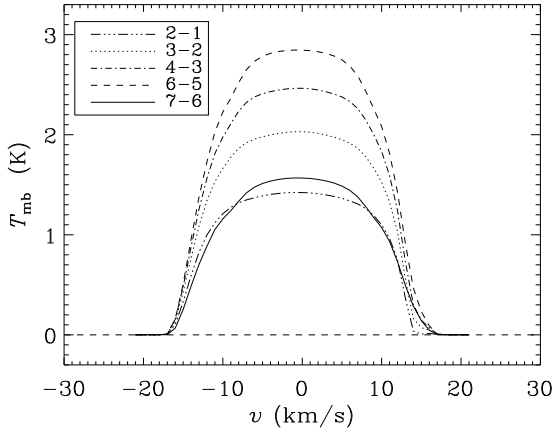


Fig. 3. Line profiles calculated for a standard AGB model, folded with the JCMT beams. The model parameters are given in Table 2.

stars. For all sources, except VY Cma, the integrated intensity increases from the CO(2–1) to (3–2) transition, and decreases again for higher transitions. This is also visible in the peak main beam temperatures T_{mb} (Table A.3). Since most studies concentrate on the lower transitions (up to CO(3–2)) this was not noticed before. An exception are the JCMT observations of OH 26.5+0.6 performed by Justtanont et al. (1996), where the CO(4–3) transition is included as well. However, as pointed out in Sect. 2.3, they observed an increasing line strength with increasing rotational transition. This differs from our observations of this object that the CO(3–2) is the strongest emission line.

In order to explain the observational trends, we have constructed a standard model assuming physical parameters widely used for AGB outflows (see Table 2). We used a mass-loss rate of $\dot{M} = 10^{-5} M_{\odot} \text{ yr}^{-1}$, and calculated the level populations of the CO gas between the stellar radius $R_{*} = 4.0 \cdot 10^{13} \text{ cm}$ and the outer radius $R_{\text{out}} = 6000 R_{*}$. For the terminal velocity we used $v_{\infty} = 15.0 \text{ km s}^{-1}$ and the turbulent velocity was assumed to be $v_{\text{sto}} = 1.0 \text{ km s}^{-1}$. A power-law temperature profile was chosen: $T(r) = 2000 (r/R_{*})^{-0.7} \text{ K}$. We used for the relative abundance of the CO gas with respect to molecular hydrogen $[\text{CO}]/[\text{H}_2] = 3.0 \cdot 10^{-4}$, and we ignored the contribution of thermal emission from dust to the local radiation field. Finally, we placed this system at a distance of 1000 pc, and used the JCMT telescope parameters to calculate the emerging line profiles (Table 2, Fig. 3). The lines show increasing peak and integrated intensities with increasing line strengths, up to CO(6–5). The CO(7–6) line is again much weaker which can be explained by the relatively narrow HPBW of the E-band (Table 1). This transition is comparable in strength to the CO(2–1) transition, for this standard set of parameters. This is a general characteristic of all other studies calculating the line intensities for com-

Table 2. Parameters of the standard AGB model

parameter	value
distance	1.0 kpc
v_{∞}	15.0 km s ⁻¹
v_{sto}	1.00 km s ⁻¹
R_{in}	5 R_{*}
R_{out}	6000 R_{*}
R_{*}	$4.0 \cdot 10^{13} \text{ cm}$
\dot{M}	$10^{-5} M_{\odot} \text{ yr}^{-1}$
$T(r)$	$2000 (r/R_{*})^{-0.7} \text{ K}$
$[\text{CO}]/[\text{H}_2]$	$3.0 \cdot 10^{-4}$
dust-to-gas ratio	0%

monly used AGB parameters (e.g. Groenewegen 1994a,b; Justtanont et al. 1994).

In the following sections we will try to find a set of parameters to explain our observations: in general the CO(3–2) is the strongest line, which contradicts the results of the standard model. In order to study as many stars as possible in a systematic way, we will use a line ratio diagram based on the CO(3–2)/CO(2–1) and CO(4–3)/CO(2–1) ratios of integrated intensities, rather than trying to fit the intensities and line profiles.

The two low mass-loss rate AGB stars RV Boo and X Her are added to the sample; these stars are the only ones for which sufficient reliable line ratios of interest can be derived from published JCMT data (see Table A.4). For RV Boo the ratios of the integrated intensities are 1.5 and 2.0 for CO(3–2)/CO(2–1) and CO(4–3)/CO(2–1) respectively (Bergman et al. 2000). For X Her these numbers are 2.1 and 3.4 respectively (Knapp et al. 1998; Kerschbaum & Olofsson 1999). The observations of Knapp et al. (1998) were obtained with the CalTech Submillimeter Observatory (CSO) and are rescaled to the JCMT observations of Kerschbaum & Olofsson (1999) such that the line intensities of the CO(3–2) transitions both reflect the same dish size and can be compared to our CO(3–2) and CO(2–1) observations. One should bear in mind however, that RV Boo and X Her are not representative of AGB stars with spherical outflows. Kahane & Jura (1996) have mapped X Her in CO lines and conclude that in addition to a slow spherically expanding shell there are indications for bipolar outflows with a higher velocity, which carry a significant fraction of the ejected gas. This result is confirmed by Kerschbaum et al. (2003), who in addition present SiO line observations indicative of a circumstellar rotating disk. Interferometric CO line observations of RV Boo indicate that this object also has a disk, possibly showing Keplerian rotation (Bergman et al. 2000). Therefore, comparison of these stars with our data and analysis should be done with some reservation.

In the literature, we found a sample of six Miras, which were observed in all three lines discussed here, using CSO (see Table A.4). It is possible to scale these observations to the JCMT observations by accounting for the dish size. However, we have chosen not to do this, because it is un-

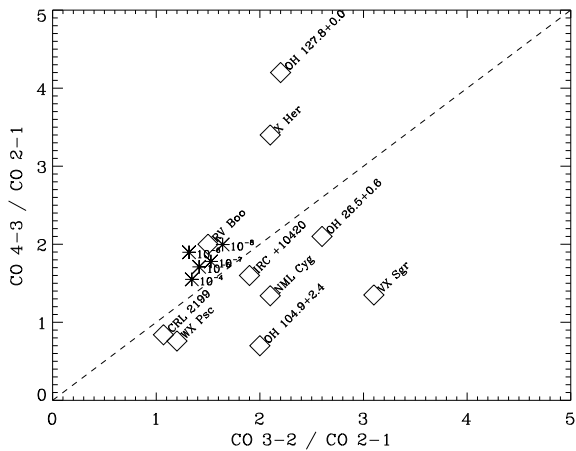


Fig. 4. Line ratio diagram. On the horizontal axis the ratio of the integrated intensities of CO(3–2)/CO(2–1) is given, while the CO(4–3)/CO(2–1) ratio is plotted on the vertical axis. The diamonds represent the positions of our sample stars, complemented with literature data for X Her and RV Boo. Equal ratios are indicated with the dashed line. In case of our sample stars, the CO(3–2) transition is stronger than the (4–3) transition, therefore all observations can be found in the lower right half of the diagram. The only exception is OH 127.8+0.0 which is found in the upper left half. The asterisks mark the positions of model calculations, where we used the standard parameters (see Table 2). Only the mass-loss rate was varied and is given in units of $M_{\odot} \text{ yr}^{-1}$.

known how reliable the rescaled data still is, as little is known about the beam filling factor of the various transitions, while the beam sizes of the telescopes are very different. Instead we chose to compare these observations with our model calculations, as will be discussed in Sect. 4.1.

4.1. A constant mass-loss rate?

In a line-ratio diagram (Fig. 4), the observed values occupy the lower right half of the diagram, corresponding to the region where the CO(3–2) line is stronger than the CO(4–3) line. The values corresponding to OH 127.8+0.0 are an exception and are found in the upper left half. This data point should be treated with care though, as the detected lines suffer from interference with interstellar absorption (Fig. A.3) and therefore the line intensities are not well known (see Table A.3). The literature data of RV Boo and X Her are also located in the upper left half of the diagram.

First, we assume that the mass-loss rate is constant. For five different mass-loss rates (10^{-8} , 10^{-7} , 10^{-6} , 10^{-5} and $10^{-4} M_{\odot} \text{ yr}^{-1}$) we have calculated the emerging line profiles, thus covering the full range in \dot{M} from Miras to OH/IR stars (Bedijn 1987; van der Veen & Habing 1988). All other input parameters were assumed to have the standard values given in Table 2. The predicted CO(3–2)/CO(2–1) and CO(4–3)/CO(2–1) ratios of the

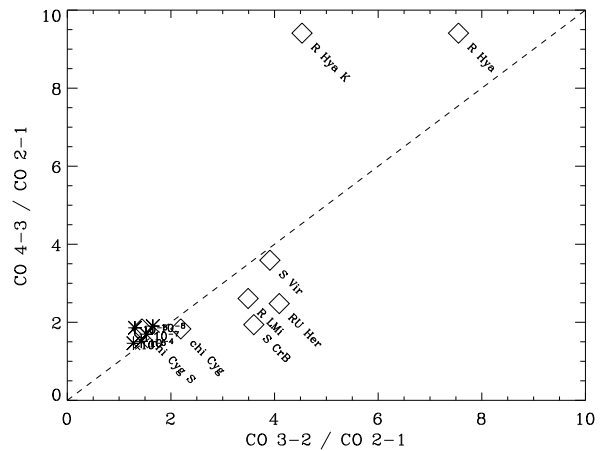


Fig. 5. Line ratio diagram for CSO data. On the horizontal axis the ratio of the integrated intensities of CO(3–2)/CO(2–1) is given, while the CO(4–3)/CO(2–1) ratio is plotted on the vertical axis. The diamonds represent the ratios obtained for a sample of six Miras. The CO(4–3) and CO(3–2) data are obtained from Young (1995), and the CO(2–1) data is taken from a study by Knapp et al. (1998). For R Hya and χ Cyg additional CSO CO(3–2) data are available, from Knapp et al. (1998) and Stanek et al. (1995) respectively. In the diagram these measurements are indicated with 'R Hya K' (Knapp et al. 1998) and an ' χ Cyg S' (Stanek et al. 1995). Equal ratios are indicated with the dashed line. The asterisks mark the positions of model calculations, performed for the CSO beam and dish size, where we used the standard parameters (see Table 2). Only the mass-loss rate was varied and is given in units of $M_{\odot} \text{ yr}^{-1}$.

integrated intensities were compared to the observed ratios.

The model calculations (marked with asterisks) are found in the upper left half of the diagram where the CO(4–3) line is stronger than the CO(3–2) line, and are therefore not consistent with the observed line ratios. All model line ratios are found in a narrow range to one end of the region where the observations are found (see Fig. 4). Only the observations of RV Boo match the modelled line ratios, but this could be merely a coincidence as RV Boo is not a typical AGB star.

There are not many reports in the literature of AGB stars observed in these three lines with the JCMT, but we compared the results discussed here with observations performed using the CSO. For that purpose, we have recalculated the model line ratios for the CSO beam and dish size. A sample of six Miras is consistently observed with CSO, where the CO(4–3) and CO(3–2) measurements are obtained by Young (1995), and the CO(2–1) observations by Knapp et al. (1998). Additional CSO observations of the CO(3–2) line in two of these objects were also included (Knapp et al. 1998; Stanek et al. 1995). The results are shown in Fig. 5. Similar to Fig. 4, the line ra-

tios derived from the standard calculations are found just above the dashed line, indicating that the CO(4–3) line should be stronger than the CO(3–2) transition. However, most observations are found well below the dashed line, where the CO(3–2) is the strongest line. χ Cyg falls in this region as well. However, if we use the measurement of Stanek et al. (1995) for the CO(3–2) line, the line ratios become such that it is found in the same region as the model ratios. Possibly this point is unreliable, as it does not come from a consistent data set. R Hya seems to be an outlier for both CO(3–2) measurements. Another remarkable observation is that the observed CO(2–1) lines seem to be weaker than what is expected from the model calculations, given the fact that the calculated ratios are closer to the origin of the plot. We may conclude that in general the CSO observations occupy more or less the same region of the plot with respect to the model ratios as our observations. Therefore, in the remainder of this paper we will limit our detailed analysis to our JCMT data.

Apparently, variations of the mass-loss rate alone do not change the line ratios enough to significantly increase the strength of the CO(3–2) line with respect to the CO(4–3) line. In the next section, we will investigate to what extent variations in the other parameters can shift the model calculations such that the line strength ratios more closely resemble the observed values.

4.2. Exploring parameter space

To further explore parameter space, we opted to vary the input parameters of the standard model (Table 2) one by one, and compare the line ratios with the observations. Combining the changes in line ratios from variations in the individual parameters then provides a feeling for the range in line ratios that can be covered, and may show whether or not it is possible to explain the observed line ratios at all. Of course, once a satisfactory match in line ratios is achieved by combining the effects of changes in individual parameters, fine tuning should be performed to fit the observed data in detail. This is necessary as some of these parameters might not be completely independent from each other, and the precise combined effect on the line profile is difficult to predict.

In Fig. 6 a mosaic of line-ratio diagrams is shown, in which the effects of changes in the stochastic velocity, the outer radius, the dust-to-gas ratio and the distance are shown. In general the effects due to changes in these parameters are small. To keep the plots readable, only small parts of the original line-ratio diagram (Fig. 4) are shown. The modelled line ratios for which these parameters are varied scatter mainly closely around the observed values for RV Boo. In all these modelled line strengths, the CO(3–2) line is still weaker than the CO(4–3) line. Of course varying the parameters mentioned here causes changes in the absolute line strengths, but the line ratios are not so much affected.

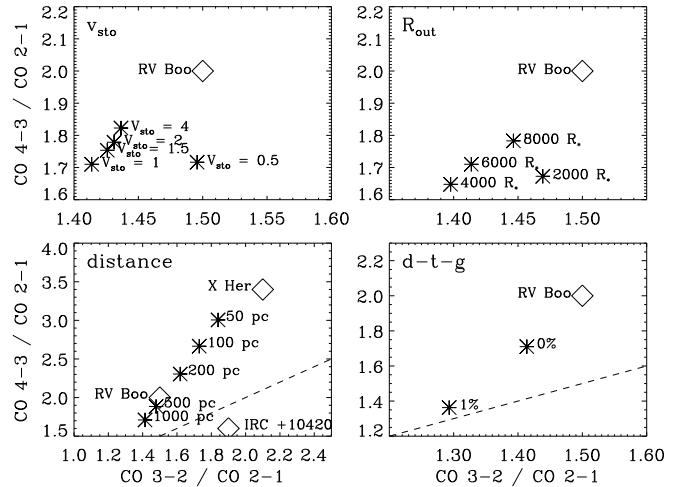


Fig. 6. Mosaic of diagrams representing the CO(4–3)/CO(2–1) ratio on the vertical axis versus the CO(3–2)/CO(2–1) ratio on the horizontal axis. We used the standard model described in Sect. 4 and Table 2 and varied for each panel one of the parameters. From the upper left corner turning clockwise the investigated parameters are: the stochastic velocity v_{sto} (km s^{-1}), the outer radius R_{out} (R_*), the dust-to-gas ratio and the distance D (pc). The line ratios resulting from the model calculations are marked with asterisks and the observed line ratios with diamonds. The dashed lines indicate equal line ratios. Note that the ranges plotted on the axes are smaller than the ranges in Fig. 4 to improve readability.

In the models where the distance was varied, we placed the object progressively closer to the observer, such that the beam filling factor is initially less than unity, but increases with decreasing distance. Although the beam size corresponding to the CO(2–1) transition is larger than that corresponding to the CO(3–2) transition, the line formation region of the CO(2–1) transition is located so much further out that the object is first resolved for the CO(2–1) transition. This implies that less emission from this line is received by the telescope. When this happens, the line ratios increase. The CO(4–3)/CO(2–1) line ratio increases faster for decreasing distance than does CO(3–2)/CO(2–1), because the CO(3–2) line emission is the next to become resolved, as this line is formed more inwards in the circumstellar shell, but still further out than the higher transitions.

The stochastic or turbulent velocity determines the interaction length along the line-of-sight, i.e. the region over which the line is formed (see also Sect. 3.1 and 3.2). The effect of a larger turbulent velocity is different for optically thick and optically thin lines. In the optically thin case, a change in profile strength may result from changes in the line source function in the (near and far) parts of the line interaction region, that is added relative to the default case. In the optically thick case the relevant source function is the one at the location where $\tau \approx 1$, which shifts towards the observer when v_{sto} is increased. It may

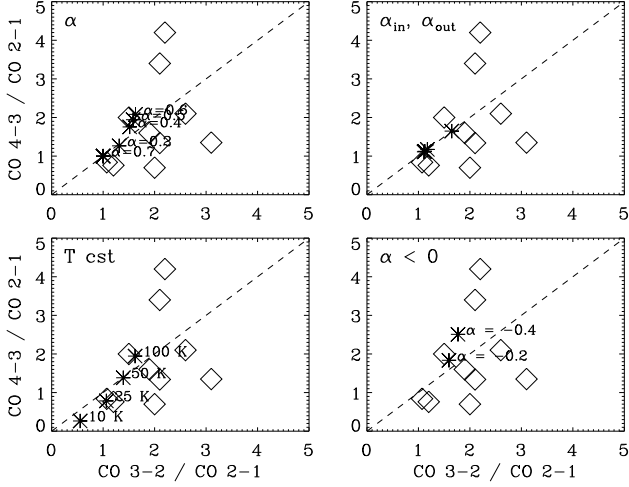


Fig. 7. Mosaic of diagrams representing the CO(4–3)/CO(2–1) ratio versus the CO(3–2)/CO(2–1) ratio. Again, the standard model parameters (Table 2) were used. Only the temperature profile was varied. From the panel in the upper left corner turning clockwise the adopted temperature profiles are: **i)** $T(r) \propto r^{-\alpha}$, with α indicated in the plot. **ii)** $T(r)$ is described with a function consisting of two power-laws. See text for description. **iii)** $T(r) \propto r^{-\alpha}$, with negative values of α , indicated in the plot. **iv)** A constant temperature throughout the circumstellar shell, where the adopted values are indicated in the plot. Again, the predicted line ratios are marked with asterisks and the observed line ratios with diamonds. The diamonds are not labelled to avoid a crowded plot, but can easily be identified using Fig. 4. The dashed lines indicate equal line ratios.

therefore differ from the default case. As these effects tend in the same direction for all lines (except possibly when lines change from optically thin to optically thick), the line ratios are found not to change dramatically when varying the turbulent velocity.

Changing the outer radius has a stronger effect on the line ratios, as can be seen in Fig. 6. When the outer radius is increased, more relatively cold gas will be present. In this gas mostly the lower rotational levels are populated, thus increasing predominantly the CO(2–1) transition. The higher the transition, the less it is affected by the outer radius.

The last parameter shown in Fig. 6 is the dust-to-gas ratio. The most important effect of adding dust to the circumstellar shell is in the population of the rotational levels. Continuum emission at $4.6 \mu\text{m}$ can be absorbed by CO molecules, exciting them from the ground to the first vibrational level. They will return to the vibrational ground state by spontaneous emission, but preferentially to a higher rotational level than they started from. This has a non-LTE effect on the level populations, leading to variations in both the line strengths and the line ratios.

We also investigated the effect of the temperature distribution. The results are shown in Fig. 7. Various tem-

Table 3. Parameters for the temperature profiles with a change in slope. See text for details.

profile	α_{in}	T_0 (K)	T_{ex} (K)
1	1.0	2500	33.1
2	1.5	2500	33.1
3	1.0	2500	16.6
4	1.0	2500	55.2
5	1.0	2200	33.1

perature profiles have been used in the different panels of this figure. The simplest approach is to consider a power law $T(r) = T_0(r/R_*)^{-\alpha}$, where α is usually positive and has a value around 0.5–0.6 for realistic profiles (Justtanont et al. 1994). We considered a much broader range of α , including negative values and also a constant temperature, i.e. $\alpha = 0$. These cases are of course not a true physical representation of the dust shell, but are just considered to study the effect of extreme conditions. In most cases, we used a temperature at the inner edge of $T_0 = 2000$ K. However, when the power law is shallow (small α), the resulting temperature at the outer radius would be higher than 25 K if we use the same value for T_0 . In that case, we adjusted T_0 such that $T(R_{\text{out}}) = 25$ K. This outer boundary temperature is in the regime of excitation temperatures of the lower rotational transitions. For the negative values of α , the temperature T_0 was assumed to be 25 K. A number of models with $\alpha = 0$ has also been computed, see the lower left panel of Fig. 7. Adopted temperatures are 10, 25, 50 and 100 K. The models with a constant temperature or an outwards increasing temperature are unrealistic, but we included them in our parameter study, to see if it is possible at all to change the line ratios significantly by changing the run of the temperature.

To add to the realism of the models, we composed a number of temperature profiles consisting of two power laws with different values for α . These profile are inspired by heat balance calculations of Justtanont et al. (1994), and are defined as follows:

$$T(r) = \begin{cases} T_0(r/R_*)^{-\alpha_{\text{in}}} & \text{for } T > T_{\text{ex}} \\ T_1(r/R_*)^{-\alpha_{\text{out}}} & \text{for } T < T_{\text{ex}} \end{cases}$$

Five different profiles with a change in slope were constructed, where the excitation temperatures of the CO(4–3) ($T_{\text{ex}} = 55.2$ K), (3–2) (33.1 K) and (2–1) (16.6 K) were used to define the position of the change in the slope. In all cases α_{out} was chosen to be 0.7. For the other parameters, the reader is referred to Table 3. The resulting line ratios are plotted in the upper right panel of Fig. 7. All models with a power law with a slope change cluster remarkably close to the CO(4–3)/CO(2–1) and CO(3–2)/CO(2–1) ratios observed in CRL 2199 and WX Psc. The only outlier is profile 2 (see Table 3). Although from the various panels in Fig. 7 it seems to be possible to explain the observed ratios of WX Psc and CRL 2199,

Table 4. Physical parameters of WX Psc. The terminal velocity v_∞ and system velocity of the object v_{LSR} are derived from our observations (Table A.3). The other parameters are extracted from the literature, the references are: ¹van Langevelde et al. (1990), ²Hofmann et al. (2001), ³Justtanont et al. (1994), ⁴Zubko & Elitzur (2000), ⁵SIMBAD, ⁶Le Sidaner & Le Bertre (1996), ⁷Lançon & Wood (2000).

parameter	value	ref.
distance	0.74 kpc	1
v_∞	20 km s ⁻¹	
v_{LSR}	+9 km s ⁻¹	
R_{in}	6.6 R_*	2
T_{eff}	2250 K	2
α	0.5	3,4
sp. type	M9-10	5
L_*	$(1.22 - 1.31) \cdot 10^4 L_\odot$	6
M_*	$> 5 M_\odot$	7

it is not possible to explain the line ratios of other stars of our sample, not even for extreme temperature profiles.

4.3. A representative case: WX Psc

In order to investigate the possibilities to explain the integrated intensities of the CO rotational transitions, we will focus on WX Psc. All transitions are observed and detected. The signal-to-noise ratio is reasonable for all transition, except for the CO(6–5) line. The previous section has shown that the line ratios of the lower rotational transitions can be explained using power law temperature profiles. In this section we expand our investigations to the higher rotational transitions. The observed values for the integrated intensities I of the CO(6–5) and (7–6) transition are much lower than the expected values based on the standard model described in Sect. 4.

WX Psc is a well studied AGB star with an intermediate mass-loss rate. From recent studies, notably the work of Hofmann et al. (2001), we have retrieved the physical characteristics of the star and the circumstellar environment (see Table 4). These values were used as input parameters for our model calculations. For required parameters which are not accurately known, we maintained the values of our standard model (Table 2). We used a stellar radius of $5.4 \cdot 10^{13}$ cm, implying a luminosity of $1.3 \cdot 10^4 L_\odot$ for $T_{\text{eff}} = 2250$ K.

Determination of the mass-loss rate from the integrated intensities of the rotational transitions gives an idea of the mass-loss history of the AGB star. Fig. 8 shows how the integrated line intensities depend on it. In Table 5 the mass-loss rates derived from each observed transition are listed, while all other parameters were kept fixed. In addition, the gas mass-loss rate, derived from the $L - [12 \mu\text{m}]$ colour (Kemper et al. 2002) is given, where a dust-to-gas ratio of 1% is assumed. The dust spectral energy distribution covers a temperature range of $\sim 200 - 800$ K, which

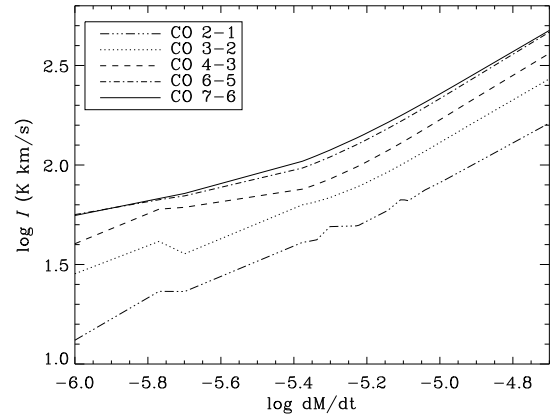


Fig. 8. Using the known parameters of WX Psc (Table 4) predicted integrated intensities are given for a large range of mass-loss rates. Integrated intensities are plotted in a logarithmic scale on the vertical axis, and mass-loss rates ($M_\odot \text{ yr}^{-1}$) on the horizontal axis, also in logarithmic scale. The integrated intensities have been calculated for all lines observable with the JCMT and these calculated models are indicated with symbols (see legend). The models have been connected with a line. Using the observed integrated intensity for a certain line, the mass-loss rate of WX Psc can be estimated from this plot (see Table 5).

corresponds to a region even more inwards than the CO line emission.

We conclude that constant mass-loss rate models cannot explain all of the observed line intensities. Rather, it seems that the mass-loss rate varies with the J -level under consideration. Specifically, the mass-loss rate corresponding to the CO(2–1) emission is almost comparable in strength to the mass-loss rate derived from the dust emission (Table 5). For the higher rotational transitions, the derived mass-loss rates go down with increasing line frequency, although it perhaps increases slightly again for the CO(7–6) transition. The mass-loss rates determined from the high rotational transitions disagree with the mass-loss rate derived from the infrared dust emission. A difference of at least an order of magnitude occurs although the regions that are traced by the high rotational transitions and the dust emission are closest in temperature, and are therefore spatially close together. In general, a decreasing mass-loss rate with increasing rotational energy level is observed, which is inconsistent with predictions based on the superwind model (e.g. Groenewegen 1994b; Justtanont et al. 1996; Delfosse et al. 1997). The results derived here point towards a mass-loss rate decreasing with time, rather than a stratification consistent with the onset of a superwind phase. In the next sections we will try to explain this discrepancy.

Table 5. Mass-loss rates for WX Psc. The values are derived for each observed transition independently. While all other parameters of WX Psc were kept constant, the mass-loss rate was determined by fitting the integrated intensity. The third column contains the excitation temperature of the corresponding rotational transition. The fourth and fifth column represent the outflow distances, i.e. the distance traveled since the gas left the stellar surface, and the last column shows the corresponding travel times. In addition to the CO mass-loss determinations, the mass-loss rate derived from the $L - [12 \mu\text{m}]$ colour, assuming a dust-to-gas ratio of 0.01, is given (Kemper et al. 2002).

tracer	\dot{M}_{gas} ($M_{\odot} \text{ yr}^{-1}$)	T_{ex} (K)	R/R_*	R (cm)	travel time (yr)
$L - [12 \mu\text{m}]$	$2.0 \cdot 10^{-5}$				< 600
CO 7-6	$3.0(\pm 0.3) \cdot 10^{-7}$	155	700	$3.8 \cdot 10^{16}$	600
CO 6-5	$1.4(\pm 0.1) \cdot 10^{-7}$	116	900	$4.9 \cdot 10^{16}$	780
CO 4-3	$1.3(\pm 0.1) \cdot 10^{-6}$	55.1	1400	$7.6 \cdot 10^{16}$	1200
CO 3-2	$6.3(\pm 0.2) \cdot 10^{-6}$	33.1	1100	$5.9 \cdot 10^{16}$	940
CO 2-1	$8.0(\pm 0.9) \cdot 10^{-6}$	16.6	1900	$1.0 \cdot 10^{17}$	1600

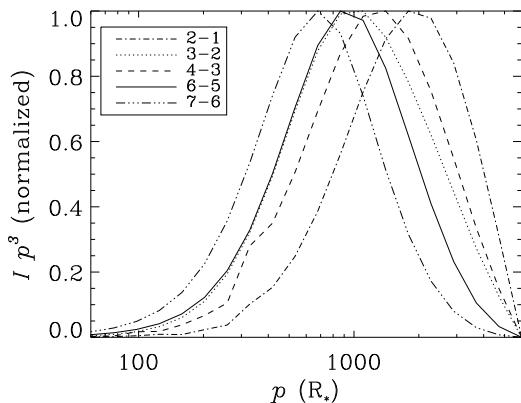


Fig. 9. Normalized intensity ($I(p)p^3$) as a function of impact parameter p . The curves for each rotational transition are calculated using the mass-loss rate corresponding to that transition (see Table 5).

4.4. Possible explanations for the inconsistency

4.4.1. Mass-loss variations?

In principle, it should be possible to construct a *combination of a density and temperature profile*, such that the observed line intensity ratios can be explained. This is not possible for a constant mass-loss rate, as becomes apparent from Fig. 7, so apparently there must also have been variations in \dot{M} . Using the WX Psc model calculations, we can derive an impression of the mass-loss history using the mass-loss rates listed in Table 5. For all these values we have calculated the region where the respective line originates (Fig. 9). This is not done in terms of radial distance to the central star, but as a function of impact parameter, in which case contributions in line-of-sights due to interactions at various radial distances have been integrated. Therefore, the values on the horizontal axis can not directly be translated to a radial distance towards the central star, but present a lower limit to this distance. In addition, one has to bear in mind that the

regions from which the various lines originate are not distinct, but largely overlap. Some overlap in Fig. 9 is due to projection effects along the line-of-sight, but a significant fraction is due to real physical overlap of the line-formation regions. Although all regions are plotted in one figure, they do not arise from the same model but are the calculated for the corresponding mass-loss rate for each line (see Table 5). Therefore, it is possible that the CO (4-3) seems to originate from a region that is more distant from the central star than the region where the CO (3-2) line originates, although their excitation temperatures would suggest otherwise in an outwards decreasing temperature profile. Concluding, the mass-loss rates that we have determined are only average values for these line formation regions. Nevertheless, estimates of the distances from the line forming regions towards the central star can be derived for the mass-loss rates traced by the observed transitions. Using a stellar radius of $5.4 \cdot 10^{13}$ cm and an expansion velocity of 20 km s^{-1} the time elapsed since the ejection of the gas from the stellar surface, traced by the various transitions can be calculated. The results are listed in Table 5. The cycle can be completed by adding the dust mass-loss, mostly originating from the region inwards of the CO(7-6) transition, and thus ejected less than 600 years ago. Note that the dust mass-loss rate is transferred into a gas mass-loss rate by assuming a dust-to-gas mass ratio of 0.01. Actual deviations to this ratio imply a different gas mass-loss rate traced by the $L - [12 \mu\text{m}]$ colour. From Table 5 we can determine that the interval between the two maximum mass-loss rates, traced by the CO(2-1) transition and the $L - [12 \mu\text{m}]$ colour of the dust emission, is of the order of ~ 1000 years.

Mass-loss variations on such time scales have in fact been observed in other evolved stars. Circumstellar series of arc-like structures have been interpreted as due to mass-loss modulations, notably for C-rich post-AGB stars, where the separation is a measure for the time scale of these variations. Kwok et al. (1998) derive that the separation between arcs observed around IRAS 17150-3224 corresponds to a time scale of

240 yr (D/kpc) ($v_{\text{exp}}/10 \text{ km s}^{-1}$). For reasonable numbers for the distance and outflow velocity one can determine that these arcs may be due to mass-loss variations on time scales of 200–1000 yr. A similar time scale (200–800 yr) is derived by Maun & Huggins (1999) for IRC+10216. The circumstellar arcs around CRL 2688 (Egg Nebula) are believed to be ejected at 75–200 yr intervals, assuming a distance of 1 kpc and an outflow velocity of 20 km s^{-1} (Sahai et al. 1998). IRAS LRS spectroscopy has shown that hot dust ($T > 500 \text{ K}$) is absent around a number of AGB stars. This is interpreted as a drop in mass-loss rate which occurred ~ 100 years ago, consistent with the spacing between the arcs observed around post-AGB stars (Marengo et al. 2001). Hydrodynamic calculations considering the gas and dust as partially or completely decoupled outflow components resulted in mass-loss variations of an order of magnitude at intervals of 200–350 year for partially and 400 year for completely decoupled fluids (Simis et al. 2001). Moreover, Fong et al. (2003) report on the discovery of multiple shells seen in CO (1–0) emission around IRC+10216. These shells are found to have intershell time scales of 1300–2900 year. The circumstellar arcs and molecular shells observed around post-AGB stars and the density enhancements emerging from hydrodynamic calculations have similar time scales to what we derive here for mass-loss variations in the outflow of WX Psc, indicating that the same phenomenon may perhaps play a role here.

Variations in the mass-loss rate of AGB stars have already been studied for a long time. It is generally accepted that the AGB phase is terminated by the superwind; a phase in which the mass-loss rate rapidly increases (Renzini 1981; Baud & Habing 1983). However, the mass-loss rates inferred from the CO line intensities for WX Psc decrease with time and are thus opposite to the classical superwind model predictions. The thermal pulses associated with He-shell ignition are also thought to cause mass-loss variations (Vassiliadis & Wood 1993). As for the superwind, the behaviour and time scale of these variations do not comply with our model predictions.

4.4.2. A gradient in the turbulent velocity?

Besides a complex density-temperature profile due to periodic mass-loss variations, there may be another way to explain the line intensities of the CO rotational transitions observed in WX Psc; a *gradient in stochastic velocity* v_{sto} . The stochastic velocity is an important parameter in the line formation process (see Sect. 3). Fig. 10 illustrates this for the profiles of one of the rotational transitions for various stochastic velocities.

Analogous to the determination of the mass-loss history, it is possible to estimate the variations in the stochastic velocities traced by the integrated intensities of the sequence of rotational transition observed for WX Psc. For this purpose, the mass-loss rate was assumed to be constant at a rate of $10^{-6} M_{\odot} \text{ yr}^{-1}$ throughout the cir-

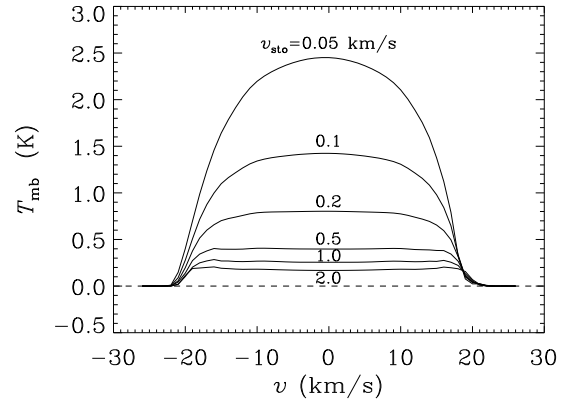


Fig. 10. The influence on the line profile of CO(3–2) due to variations of the stochastic velocity. The input parameters of our standard model are used (Table 2), only the turbulent velocity – which in our model is independent of r – is varied, in the range from $0.05 - 2.0 \text{ km s}^{-1}$.

Table 6. Stochastic velocities for WX Psc. The values are derived for each observed transition independently, while all other parameters were kept constant. The stochastic velocities were determined by fitting the integrated intensities.

tracer	v_{sto} (km s^{-1})
CO(7–6)	3.2 ± 0.4
CO(6–5)	8 ± 1
CO(4–3)	1.0 ± 0.1
CO(3–2)	0.24 ± 0.04
CO(2–1)	0.16 ± 0.05

cumstellar outflow. The temperature profile and the other parameters were kept the same as the ones used in the mass-loss history analysis. The results are listed in Table 6. Again, the line formation regions and thus the values derived here are not independent and should be seen as averages over the formation regions. The observed line intensities may be explained by a gradient in the stochastic velocity if it is lowest in the outer parts of the outflow, traced by the low rotational transitions, and has its maximum in the gas traced by the CO(6–5) transition.

One has to bear in mind that we derived the stochastic velocities for one particular mass-loss rate, namely $10^{-6} M_{\odot}$. As pointed out before, the mass-loss rate has a considerable effect on the line strengths as well, however, the negative gradient will be maintained for other choices of \dot{M} . To explain the observations v_{sto} has to increase to an unrealistically high maximum of 8 km s^{-1} in the region of CO(6–5) formation and then decrease again to 0.16 km s^{-1} at the CO(2–1) formation zone.

The stochastic velocity can be considered as a composition of thermal and turbulent components, according to Eq. (2). The thermal molecular velocities for CO are given

by $v_{\text{therm}} = \sqrt{2kT/m_{\text{CO}}}$, where T is the temperature at the line formation region, which is usually of the order of the excitation temperature. For the lines observed we can determine that v_{therm} ranges between 0.01 and 0.03 km s⁻¹. It is obvious that only a minor fraction of the required total stochastic velocity v_{sto} can be explained by thermal motion, and also that the observed gradient is not sufficiently reproduced by the thermal component.

The nature of the remaining turbulent velocity v_{turb} is unknown, but could in part be induced by stellar pulsations. These pulsations cause stochastic velocities of 2–5 km s⁻¹ in the inner parts of the circumstellar shell required to start the dust formation process. However, these stochastic velocities will damp quickly and are practically absent beyond 100 R_* (Simis 2001). Hence, if variations in the stochastic velocity are important for the CO line intensities, the origin of such variations is presently unclear.

4.4.3. Other factors

Other factors that could be important include the outflow velocity profile, and the geometry. Our adopted outflow velocity profile is very simple (see Eq. (4)), but hydrodynamical calculations show that it may be more complex and also time-dependent (Simis et al. 2001). The effect of such complex outflow velocity profiles on the CO line profiles has not yet been studied. Perhaps they could serve as a source of turbulence.

Non-spherical winds, e.g. density enhancements in the equatorial region, could also play a role in the observed line strengths. The observed line profiles would reflect such an axi-symmetric geometry, if it exists. Close examination of the observed lines (Figs. A.1–A.21) shows that their profiles are similar for all transitions (per source), and one can therefore conclude that the regions where the lines originate have almost the same velocity structure. Apparently there is no change in geometry for the regions traced by the various rotational transitions, e.g. a slowly outflowing disk traced by the lower transitions and a fast polar outflow traced by the higher transitions. Thus this possibility most likely can be ruled out as an explanation for the discrepancy between the observations and the model results. Only in case of VY CMa (Fig. A.9) the profiles show significant differences between the lower and higher rotational transitions.

5. Concluding remarks

5.1. CO rotational transitions as mass-loss indicators

In this work, we presented submillimeter observations of various carbon monoxide rotational transitions (CO(7–6), (6–5), (4–3), (3–2), (2–1)) observed in AGB stars and red supergiants in various evolutionary states. We have attempted to determine the mass-loss history of the programme stars by modelling of the observed transitions. For the first time the CO(7–6) and (6–5)

transitions were used, in addition to lower transitions. In this way the gap between the regions in the outflow traced by the gas and that traced by the dust emission was largely closed. Many studies in the past have focussed on only one or two transitions to determine the gas mass-loss rate (e.g. Knapp & Morris 1985; Loup et al. 1993; Justtanont et al. 1994; Groenewegen 1994b; Justtanont et al. 1996; Delfosse et al. 1997). The extension of the data towards higher rotational transitions clearly demonstrates that determination of a unique gas mass-loss rate from a single CO rotational transition is highly unreliable. We found that the observed line strengths indicate that the outflow has a more complex physical structure than was previously assumed. Not a superwind, but periodic mass-loss variations comparable to the arc-like structures and rings observed around post-AGB stars, may possibly account for the observed line strengths. Part of the discrepancy could be due to a gradient in the stochastic velocity as well.

Independently, another research group has reached the same conclusion during the last year. Initially, Olofsson et al. (2002) modelled the mass-loss rates of a large sample of irregular and semi-regular M-type variables by fitting 2, 3 or in one case 4 CO rotational transitions by assuming a constant mass-loss rate over the last 1000 years. They derive rates for their sample stars and do not report on problems similar to ours, but their figures 2 and 11 show that the line strength of the higher transitions is overestimated when this model is used. In the same volume of A&A, Schöier et al. (2002) describe a model that is able to use periodic mass-loss variations to calculate the rotational transitions of CO in C-rich stars. The development of this model is driven by the discovery of mass-loss modulations. However, after thorough analysis, they conclude that mass-loss modulations are not important nor necessary to explain the CO rotational line profiles. The most recent results of González Delgado et al. (2003) indicate otherwise, however. When trying to derive the mass loss rate of more evolved Miras (i.e. with higher mass-loss rates than the semi-regulars), González Delgado et al. (2003) find that a model assuming a constant mass-loss rate underestimates the strength of the low transitions. This is in principle the same as our result that the high transitions are overestimated.

5.2. Future work

The work presented here has revealed a much more complex picture of AGB stellar ejecta than previously assumed. Additional research is required, which we plan to do in the near future. Of particular importance are the following issues:

- First, more observational data should be obtained, in particular of high rotational transitions. Our study is the first to include the CO(6–5) and (7–6) transitions in the mass-loss rate determinations of three evolved stars. In addition, for one object (NML Cyg) observa-

tions up to CO(6–5) were secured. This is not enough to draw firm conclusions on the degree of complexity of the physical structure in the outflows of AGB stars, therefore this sample should be enlarged. It is important to pay attention to the completeness: if all transitions are observed, variations in the important physical parameters can be much better constrained. In that respect it is also worthwhile to extend the data with observations of ^{13}CO for the lower transitions, which provide additional independent constraints on the physical conditions.

- Second, a more realistic representation of the physical conditions in the outflow of AGB stars should be used. This includes adding a gradient in turbulence and periodic mass-loss variations as we have argued in this study. In addition, the velocity law could also be improved, e.g. following the results of Simis et al. (2001). Although these adjustments will lead to an increase in the number of free parameters, it is likely that we will be able to use the *line profiles* to constrain the model parameters. This will certainly help in disentangling the physical structure of the outflow.

Acknowledgements. FK is grateful for the hospitality at the Stockholm Observatory. The support provided by the staff of the JCMT is greatly appreciated. The James Clerk Maxwell Telescope is operated on behalf of the Particle Physics and Astronomy Research Council of the United Kingdom, the Netherlands Organisation for Scientific Research and the National Research Council of Canada. This research has made use of the SIMBAD database, operated at CDS, Strasbourg, France. FK, AdK and LBFMW acknowledge financial support from NWO ‘Pionier’ grant 616-78-333. Support for this work was provided by NASA through the SIRTf Fellowship Program, under award 011 808-001.

References

- Baud, B. & Habing, H. J. 1983, *A&A*, 127, 73
 Bedijn, P. J. 1987, *A&A*, 186, 136
 Bergman, P., Kerschbaum, F., & Olofsson, H. 2000, *A&A*, 353, 257
 Cami, J., de Jong, T., Justtanont, K., Yamamura, I., & Waters, L. B. F. M. 1998, *Ap&SS*, 255, 339
 Chen, W. & Neufeld, D. A. 1995, *ApJ*, 453, L99
 Danchi, W. C., Green, W. H., Hale, D. D. S., et al. 2001, *ApJ*, 555, 405
 Delfosse, X., Kahane, C., & Forveille, T. 1997, *A&A*, 320, 249
 Dijkstra, C., Waters, L. B. F. M., Kemper, F., et al. 2003, *A&A*, 399, 1037
 Flower, D. R. & Launay, J. M. 1985, *MNRAS*, 214, 271
 Fong, D., Justtanont, K., Meixner, M., & Campbell, M. T. 2002, *A&A*, 396, 581
 Fong, D., Meixner, M., & Shah, R. Y. 2003, *ApJ*, 582, L39
 Gehr, R. 1989, in *IAU Symp. 135: Interstellar Dust*, ed. L. J. Allamandola & A. G. G. M. Tielens, 445–453
 Goldreich, P. & Scoville, N. 1976, *ApJ*, 205, 144
 González Delgado, D., Olofsson, H., Kerschbaum, F., Schöier, F. L., & Lindqvist, M. 2003, *A&A*, in press
 Groenewegen, M. A. T. 1994a, *A&A*, 290, 531
 —. 1994b, *A&A*, 290, 544
 Habing, H. 1996, *A&A Rev.*, 7, 97
 Herman, J., Burger, J. H., & Penninx, W. H. 1986, *A&A*, 167, 247
 Heske, A., Forveille, T., Omont, A., van der Veen, W. E. C. J., & Habing, H. J. 1990, *A&A*, 239, 173
 Hofmann, K.-H., Balega, Y., Blöcker, T., & Weigelt, G. 2001, *A&A*, 379, 529
 Hyland, A. R., Becklin, E. E., Frogel, J. A., & Neugebauer, G. 1972, *A&A*, 16, 204
 Iben Jr., I. & Renzini, A. 1983, *ARA&A*, 21, 271
 Jackson, B. D., de Lange, G., Laauwen, W. M., et al. 2000, in *Proc. of the 11th Int. Symp. on Space THz Technology*, 238
 Jones, T. J., Humphreys, R. M., Gehr, R. D., et al. 1993, *ApJ*, 411, 323
 Justtanont, K., Skinner, C. J., & Tielens, A. G. G. M. 1994, *ApJ*, 435, 852
 Justtanont, K., Skinner, C. J., Tielens, A. G. G. M., Meixner, M., & Baas, F. 1996, *ApJ*, 456, 337
 Kahane, C. & Jura, M. 1996, *A&A*, 310, 952
 Kemper, F., de Koter, A., Waters, L. B. F. M., Bouwman, J., & Tielens, A. G. G. M. 2002, *A&A*, 384, 585
 Kemper, F., Waters, L. B. F. M., de Koter, A., & Tielens, A. G. G. M. 2001, *A&A*, 369, 132
 Kerschbaum, F. & Olofsson, H. 1999, *A&AS*, 138, 299
 Kerschbaum, F., Olofsson, H., Posch, T., et al. 2003, *Rev. Mod. Astr.*, in press
 Knapp, G. R. & Morris, M. 1985, *ApJ*, 292, 640
 Knapp, G. R., Young, K., Lee, E., & Jorissen, A. 1998, *ApJS*, 117, 209
 Kwok, S., Su, K. Y. L., & Hrivnak, B. J. 1998, *ApJ*, 501, L117
 Lançon, A. & Wood, P. R. 2000, *A&AS*, 146, 217
 Le Sidaner, P. & Le Bertre, T. 1996, *A&A*, 314, 896
 Loup, C., Forveille, T., Omont, A., & Paul, J. F. 1993, *A&AS*, 99, 291
 Marengo, M., Ivezić, Ž., & Knapp, G. R. 2001, *MNRAS*, 324, 1117
 Maun, N. & Huggins, P. J. 1999, *A&A*, 349, 203
 Mihalas, D., Kunasz, P. B., & Hummer, D. G. 1975, *ApJ*, 202, 465
 Molster, F. J., Waters, L. B. F. M., Tielens, A. G. G. M., & Barlow, M. J. 2002, *A&A*, 382, 184
 Morris, M. 1980, *ApJ*, 236, 823
 Olofsson, H., González Delgado, D., Kerschbaum, F., & Schöier, F. L. 2002, *A&A*, 391, 1053
 Perryman, M. A. C. & ESA. 1997, *The HIPPARCOS and TYCHO catalogues. Astrometric and photometric star catalogues derived from the ESA HIPPARCOS Space Astrometry Mission, ESA-SP 1200 (Noordwijk, The Netherlands: ESA Publications Division)*
 Renzini, A. 1981, in *Physical processes in red giants*, ed. I. Iben Jr. & A. Renzini (Dordrecht, Holland: D. Reidel Publishing Company), 431–446

Sahai, R., Trauger, J. T., Watson, A. M., et al. 1998, ApJ, 493, 301
 Schöier, F. L., Ryde, N., & Olofsson, H. 2002, A&A, 391, 577
 Schönberg, K. 1988, A&A, 195, 198
 Schönberg, K. & Hempe, K. 1986, A&A, 163, 151
 Simis, Y. J. W. 2001, PhD thesis, Leiden University, The Netherlands
 Simis, Y. J. W., Icke, V., & Dominik, C. 2001, A&A, 371, 205
 Skinner, C. J., Meixner, M., Barlow, M. J., et al. 1997, A&A, 328, 290
 Stanek, K. Z., Knapp, G. R., Young, K., & Phillips, T. G. 1995, ApJS, 100, 169
 Sylvester, R. J., Kemper, F., Barlow, M. J., et al. 1999, A&A, 352, 587
 van der Veen, W. E. C. J. & Habing, H. J. 1988, A&A, 194, 125
 van Langevelde, H. J., van der Heiden, R., & van Schooneveld, C. 1990, A&A, 239, 193
 Vassiliadis, E. & Wood, P. R. 1993, ApJ, 413, 641
 Waters, L. B. F. M., Molster, F. J., de Jong, T., et al. 1996, A&A, 315, L361
 Young, K. 1995, ApJ, 445, 872
 Yuasa, M., Unno, W., & Magono, S. 1999, PASJ, 51, 197
 Zubko, V. & Elitzur, M. 2000, ApJ, 544, L137

Table A.1. Programme stars. Distances are taken from ^aHipparcos (Perryman & ESA 1997), ^bvan Langevelde et al. (1990), ^cHyland et al. (1972), ^dYuasa et al. (1999), ^eHerman et al. (1986), ^fJones et al. (1993), ^gDanchi et al. (2001)

object	α (J2000)	δ (J2000)	D (kpc)
T Cet	00 21 46.27	-20 03 28.9	0.238 ^a
WX Psc	01 06 25.99	+12 35 53.4	0.74 ^b
OH 127.8+0.0	01 33 51.19	+62 26 53.4	2.90 ^b
<i>o</i> Cet	02 19 20.793	-02 58 39.51	0.128 ^a
IRC+50137	05 11 19.37	+52 52 33.7	0.820 ^c
α Ori	05 55 10.305	+07 24 25.43	0.131 ^a
VY CMa	07 22 58.33	-25 46 03.2	0.562 ^a
α Sco	16 29 24.461	-26 25 55.21	0.185 ^a
V438 Oph	17 14 39.78	+11 04 10.0	
AFGL 5379	17 44 23.89	-31 55 39.11	1.19 ^d
VX Sgr	18 08 04.05	-22 13 26.6	0.330 ^a
CRL 2199	18 35 46.9	+05 35 48	2.48 ^d
OH 26.5+0.6	18 37 32.52	-05 23 59.4	1.37 ^b
OH 30.1-0.7	18 48 41.5	-02 50 29	1.77 ^e
OH 32.8-0.3	18 52 22.19	-00 14 13.9	5.02 ^b
OH 44.8-2.3	19 21 36.56	+09 27 56.3	1.13 ^b
IRC+10420	19 26 48.09	+11 21 16.7	5 ^f
NML Cyg	20 46 25.7	+40 06 56	1.22 ^g
μ Cep	21 43 30.461	+58 46 48.17	1.613 ^a
IRAS21554+6204	21 56 58.3	+62 18 43	2.03 ^d
OH 104.9+2.4	22 19 27.9	+59 51 22	2.30 ^b

Appendix A: Observations — Tables & Figures

Table A.2. Details of the observations. For each source the observed transitions are listed, together with the integrated observing time in seconds. The correction factor f has been applied to our measurements, derived from standard measurements. The last column lists the observing dates.

object	transition	t_{int} (s)	f	obs. date
T Cet	CO(2–1)	1800	1.07	03-Sep-02
WX Psc	CO(2–1)	1800	0.90	22-Mar-01
	CO(3–2)	1200	1	02-Jul-00
	CO(4–3)	4800	1	21-Apr-00
	CO(6–5)	7320	–	10-Oct-01
	CO(7–6)	7200	–	09-Oct-01
OH 127.8+0.0	CO(2–1)	1200	1.09	03-Sep-02
	CO(3–2)	2400	1	02-Jul-00
	CO(4–3)	5600	1	13-Apr-00
<i>o</i> Cet	CO(2–1)	600	1.08	03-Sep-02
	CO(3–2)	600	1	02-Jul-00
IRC+50137	CO(2–1)	1800	0.96	06-Dec-00
	CO(3–2)	2400	1.10	05-Dec-00
α Ori	CO(3–2)	5400	1	02-Jul-00
VY CMa	CO(2–1)	3600	1	22-Mar-01
	CO(3–2)	2400	1.10	05-Dec-00
	CO(6–5)	8400	–	10-Oct-01
	CO(7–6)	5400	–	09-Oct-01
α Sco	CO(3–2)	1800	1.10	04-Jul-00
V438 Oph	CO(2–1)	1800	1.01	03-Sep-02
AFGL 5379	CO(3–2)	1200	1	17-Apr-00
VX Sgr	CO(2–1)	1860	1	22-Mar-01
	CO(3–2)	2400	1	18-Apr-00
	CO(4–3)	2400	1	04-Jul-00
CRL 2199	CO(2–1)	1800	1	22-Mar-01
	CO(3–2)	1200	1	17-Apr-00
	CO(4–3)	8400	1	21-Apr-00
OH 26.5+0.6	CO(2–1)	1800	0.95	22-Mar-01
	CO(3–2)	1200	1	17-Apr-00
	CO(4–3)	8400	1	21-Apr-00
OH 30.1–0.7	CO(3–2)	1020	1	06-Jul-00
OH 32.8–0.3	CO(3–2)	1200	1	18-Apr-00
OH 44.8–2.3	CO(3–2)	2400	1	07-Jul-00
IRC+10420	CO(2–1)	1800	0.95	22-Mar-01
	CO(3–2)	1200	1	17-Apr-00
	CO(4–3)	2400	1	21-Apr-00
NML Cyg	CO(2–1)	1800	0.90	22-Mar-01
	CO(3–2)	1200	1	17-Apr-00
	CO(4–3)	1200	1	21-Apr-00
	CO(6–5)	4800	–	10-Oct-01
μ Cep	CO(2–1)	1800	1	20-Sep-02
	CO(3–2)	1200	1	18-Apr-00
IRAS 21554+6204	CO(2–1)	1920	1	20-Sep-02
	CO(3–2)	3600	1	07-Jul-00
OH 104.9+2.4	CO(2–1)	2400	0.90	22-Mar-01
	CO(3–2)	2400	1	18-Apr-00
	CO(4–3)	4800	1.16	13-Apr-00
		2160	1	21-Apr-00
	CO(6–5)	11400	–	10-Oct-01
	CO(7–6)	2400	–	09-Oct-01

Table A.3. Overview of observed line parameters. For each observed transition, the peak intensity (T_{mb}) is measured, together with the r.m.s. values (Col. 4) and corresponding bin sizes (Col. 5). Cols. 6 and 7 represent the velocity of the object (v_{LSR}) and the terminal velocity (v_{∞}). The integrated line intensity (Col. 8) is determined by removing interstellar absorption and emission from the profile, and integrating the remaining line profile. The accuracy on these values is at least 10% for the CO(2–1), (3–2) and (4–3) transitions and at least 30% for the CO(6–5) and (7–6) transitions. In some cases the accuracy is deteriorated due to interstellar contamination.

object	transition	T_{mb} (K)	r.m.s. (K)	bin (MHz)	V_{LSR} (km s $^{-1}$)	V_{∞} (km s $^{-1}$)	I (K km s $^{-1}$)
T Cet	CO(2–1)	0.44	0.056	0.3125	+23.1 ± 0.5	6.7 ± 0.5	3.9 ± 0.4
WX Psc	CO(2–1)	2.35	0.034	0.6250	+9.0 ± 0.5	20.2 ± 0.5	66 ± 7
	CO(3–2)	2.91	0.043	1.2500	+9.2 ± 0.5	20.3 ± 0.5	82 ± 8
	CO(4–3)	1.86	0.090	0.9375	+9.0 ± 0.5	20.6 ± 0.5	50 ± 5
	CO(6–5)	0.45	0.224	2.5000	+8.4 ± 1.5	17 ± 3	10 ± 5
	CO(7–6)	0.82	0.378	3.1250	+9.8 ± 1.5	21 ± 3	23 ± 11
OH 127.8+0.0	CO(2–1)	0.28	0.048	0.6250	−56 ± 3	13 ± 2	5.5 ± 1.6
	CO(3–2)	0.68	0.050	0.6250	−55 ± 3	13 ± 2	12 ± 1
	CO(4–3)	0.15	0.057	1.5625	complex	complex	23 ± 2
α Cet	CO(2–1)	13.80	0.170	0.1562	+46.3 ± 0.1	8 ± 1	64 ± 6
	CO(3–2)	21.61	0.134	0.3125	+46.4 ± 0.1	8 ± 2	108 ± 11
IRC+50137	CO(2–1)	1.37	0.033	0.4688	+2.8 ± 0.5	19.1 ± 0.5	37 ± 4
	CO(3–2)	1.44	0.047	0.9375	+3.2 ± 0.5	18.5 ± 0.5	39 ± 4
α Ori	CO(3–2)	complex	0.043	0.3125	+3.4 ± 0.5	15.7 ± 0.5	50 ± 5
VY CMa	CO(2–1)	complex	0.033	0.6250	+25 ± 3	47 ± 3	66 ± 7
	CO(3–2)	3.00	0.043	1.2500	+25 ± 3	47 ± 3	173 ± 17
	CO(6–5)	4.37	0.469	3.7500	+27 ± 2	48 ± 3	257 ± 77
α Sco	CO(7–6)	7.41	0.908	3.7500	+29 ± 2	44 ± 3	433 ± 130
	CO(3–2)	–	0.036	1.8750	–	–	–
V438 Oph	CO(2–1)	0.24	0.058	0.3125	+9.7 ± 0.5	4.3 ± 1.0	1.1 ± 0.2
AFGL 5379	CO(3–2)	2.76	0.056	1.2500	−22.7 ± 1.5	24 ± 2	84 ± 8
VX Sgr	CO(2–1)	complex	0.048	0.4688	+6.4 ± 1.0	25 ± 1	31 ± 3
	CO(3–2)	2.37	0.059	0.6250	+6.9 ± 1.0	26 ± 1	97 ± 10
	CO(4–3)	1.22	0.237	1.2500	+6.4 ± 0.5	22 ± 2	42 ± 4
CRL 2199	CO(2–1)	1.16	0.033	0.6250	+33.7 ± 0.2	17.6 ± 0.5	26 ± 3
	CO(3–2)	1.25	0.034	1.2500	+33.5 ± 0.2	17.9 ± 0.5	28 ± 3
	CO(4–3)	0.98	0.066	1.2500	+33.2 ± 0.5	18 ± 1	22 ± 2
OH 26.5+0.6	CO(2–1)	contamin.	0.049	0.3125	contamin.	contamin.	9 ± 3
	CO(3–2)	1.05	0.046	0.9375	+26.9 ± 0.5	18 ± 1	23 ± 2
	CO(4–3)	0.86	0.051	0.9375	+27.7 ± 0.3	15.9 ± 0.5	19 ± 2
OH 30.1–0.7	CO(3–2)	contamin.	0.076	0.9375	contamin.	contamin.	contamin.
OH 32.8–0.3	CO(3–2)	contamin.	0.047	0.9375	contamin.	contamin.	contamin.
OH 44.8–2.3	CO(3–2)	0.63	0.047	0.9375	−70.3 ± 0.2	17.7 ± 0.5	15 ± 2
IRC+10420	CO(2–1)	1.65	0.034	0.4688	+75 ± 1	43 ± 3	95 ± 10
	CO(3–2)	3.23	0.075	0.9375	+75 ± 1	45 ± 3	180 ± 18
	CO(4–3)	2.84	0.078	1.8750	+76.1 ± 0.5	42 ± 2	150 ± 15
NML Cyg	CO(2–1)	complex	0.039	0.3125	−2 ± 3	33 ± 3	99 ± 10
	CO(3–2)	complex	0.104	0.6250	−2 ± 3	33 ± 3	210 ± 21
	CO(4–3)	complex	0.106	1.2500	−1 ± 2	34 ± 2	133 ± 13
	CO(6–5)	complex	0.232	2.5000	+2 ± 2	34 ± 2	111 ± 56
μ Cep	CO(2–1)	complex	0.025	1.2500	+22 ± 2	33 ± 3	2.5 ± 0.3
	CO(3–2)	complex	0.066	0.9375	+21 ± 3	35 ± 3	14 ± 3
IRAS 21554+6204	CO(2–1)	0.58	0.041	0.4688	−19 ± 1	19 ± 2	12 ± 1
	CO(3–2)	0.49	0.036	0.9375	−19.0 ± 0.5	18.1 ± 0.5	10 ± 1
OH 104.9+2.4	CO(2–1)	0.21	0.026	0.6250	−26 ± 1	18.6 ± 0.5	5.4 ± 0.5
	CO(3–2)	0.43	0.043	0.9375	−25 ± 1	18.3 ± 0.5	11 ± 1
	CO(4–3)	0.11	0.042	1.8455	−26 ± 1	18 ± 1	3.6 ± 0.5
	CO(6–5)	–	0.224	3.7500	–	–	–
	CO(7–6)	–	1.011	3.1250	–	–	–

Table A.4. Observed CO line transitions in semi-regular variables and AGB stars, obtained from the literature. The listed stars are observed in CO(4–3), CO(3–2) and CO(2–1). The references are ^aBergman et al. (2000), ^bKerschbaum & Olofsson (1999), ^cKnapp et al. (1998), ^dYoung (1995), ^eStaneek et al. (1995).

source	line	$I(\text{K km s}^{-1})$	telescope	ref.
RV Boo	CO(4–3)	8.87	JCMT	a
	CO(3–2)	6.81	JCMT	a
	CO(2–1)	4.47	JCMT	a
X Her	CO(4–3)	42.17	JCMT	b
	CO(3–2)	25.69	JCMT	b
	CO(3–2)	13.3 ± 1.3	CSO	c
R LMi	CO(2–1)	6.4 ± 0.4	CSO	c
	CO(4–3)	7.1	CSO	d
	CO(3–2)	9.5	CSO	d
R Hya	CO(2–1)	2.72 ± 0.38	CSO	c
	CO(4–3)	46.1	CSO	d
	CO(3–2)	37	CSO	d
S Vir	CO(3–2)	22.2 ± 2.2	CSO	c
	CO(2–1)	4.9 ± 0.5	CSO	c
	CO(4–3)	2.3	CSO	d
S CrB	CO(3–2)	2.5	CSO	d
	CO(2–1)	0.64 ± 0.25	CSO	c
	CO(4–3)	4.9	CSO	d
RU Her	CO(3–2)	9.1	CSO	d
	CO(2–1)	2.53 ± 0.51	CSO	c
	CO(4–3)	5.7	CSO	d
χ Cyg	CO(3–2)	9.4	CSO	d
	CO(2–1)	2.3 ± 0.2	CSO	c
	CO(4–3)	52.7	CSO	d
	CO(3–2)	63	CSO	d
	CO(3–2)	41.5	CSO	e
	CO(2–1)	28.8 ± 0.7	CSO	c

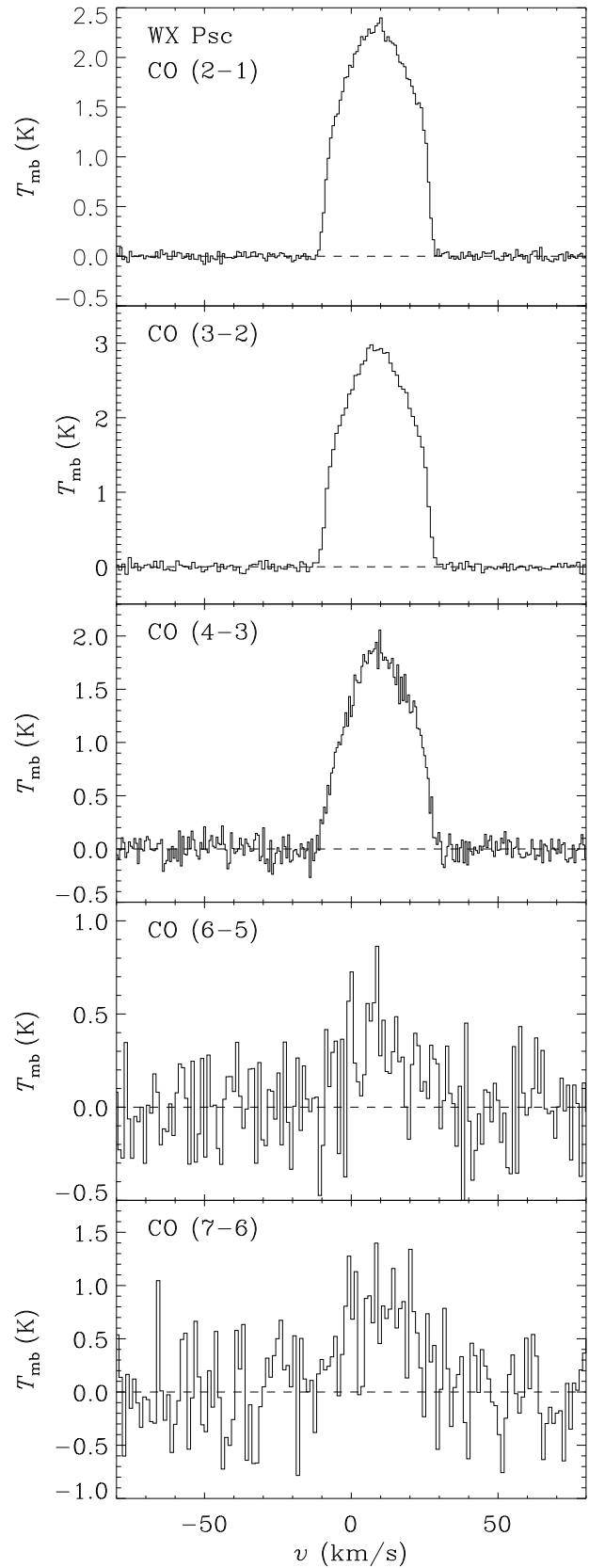


Fig. A.1. JCMT observations of rotational transitions of CO observed in WX Psc. See text for details on data reduction and analysis.

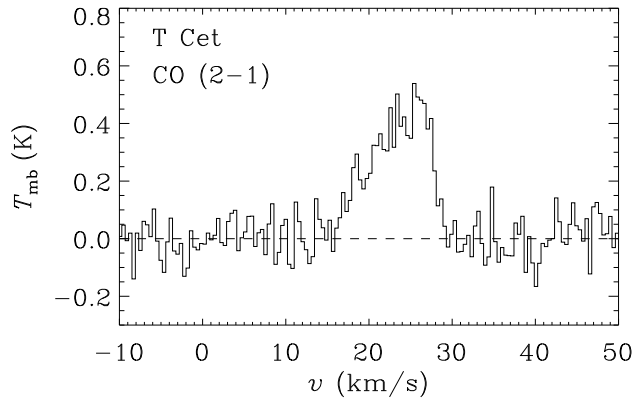


Fig. A.2. Idem – T Cet

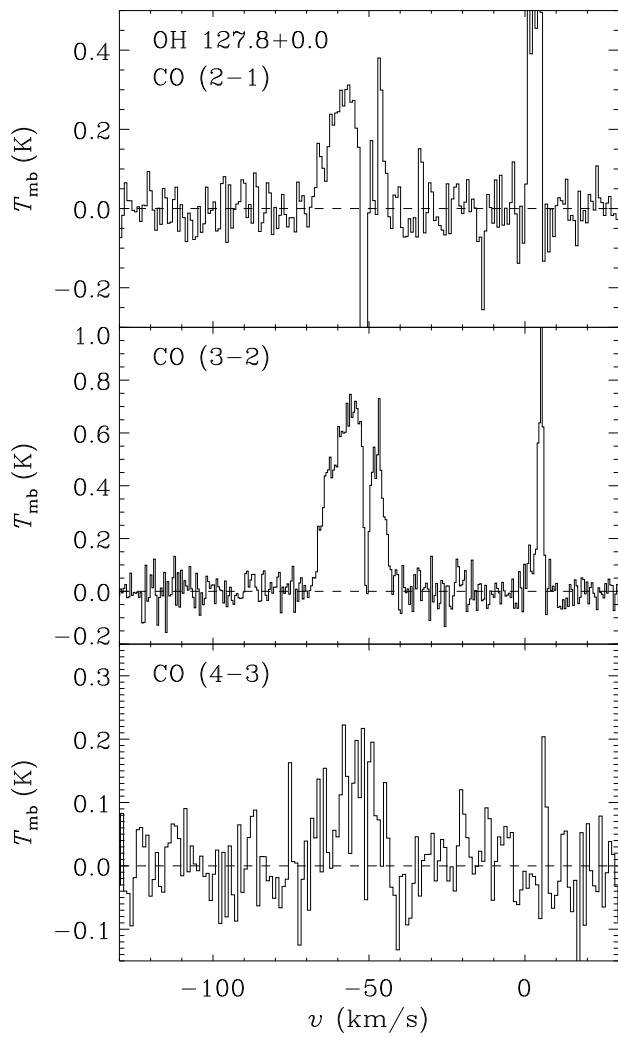


Fig. A.3. Idem – OH 127.8+0.0

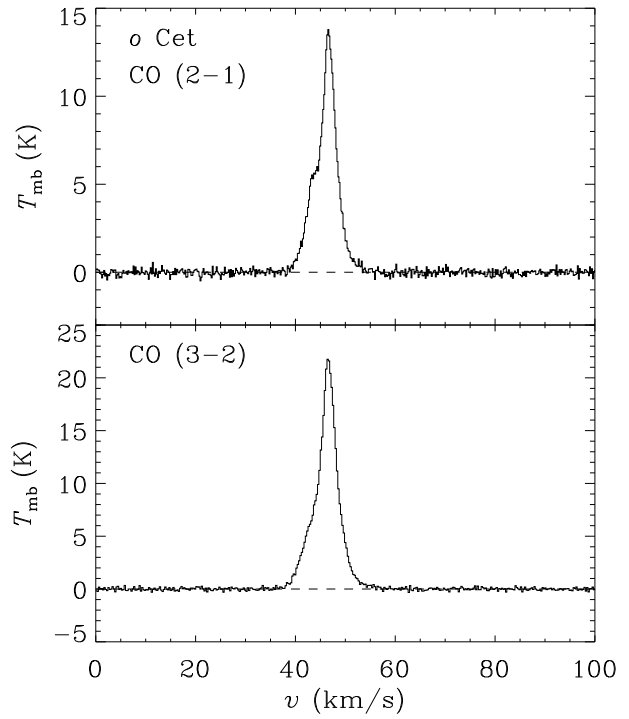


Fig. A.4. Idem – *o* Cet

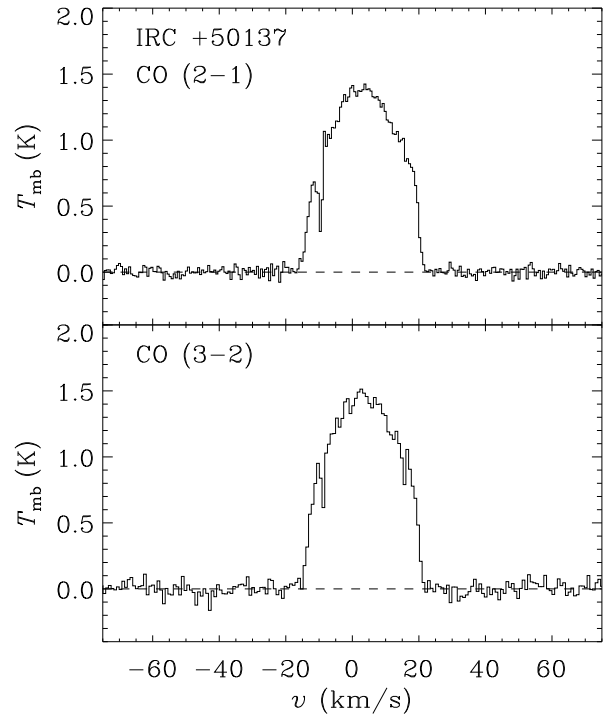


Fig. A.5. Idem – IRC +50137

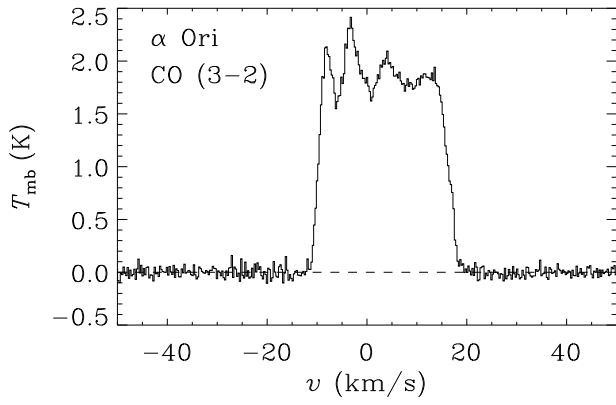
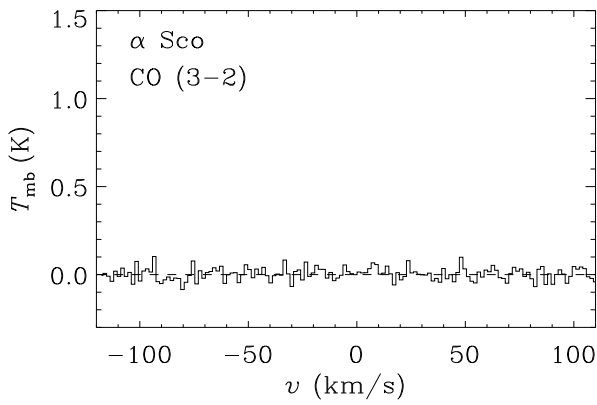
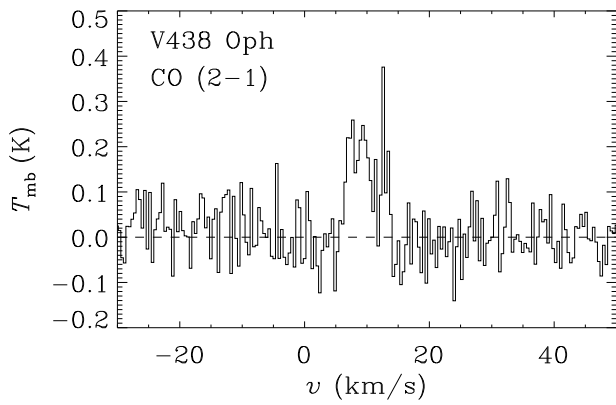
Fig. A.6. Idem – α OriFig. A.7. Idem – α Sco

Fig. A.8. Idem – V438 Oph

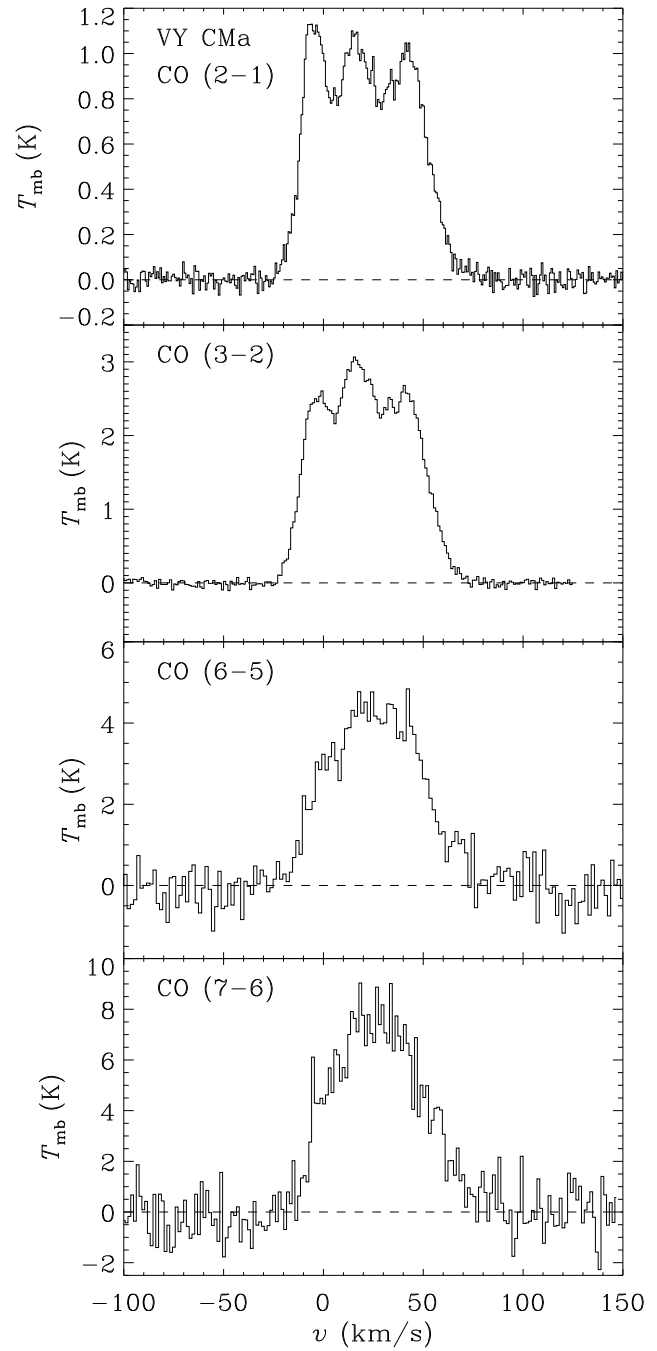


Fig. A.9. Idem – VY CMa

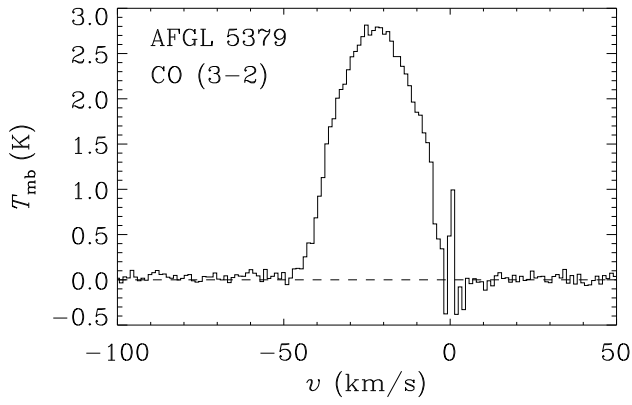


Fig. A.10. Idem – AFGL 5379

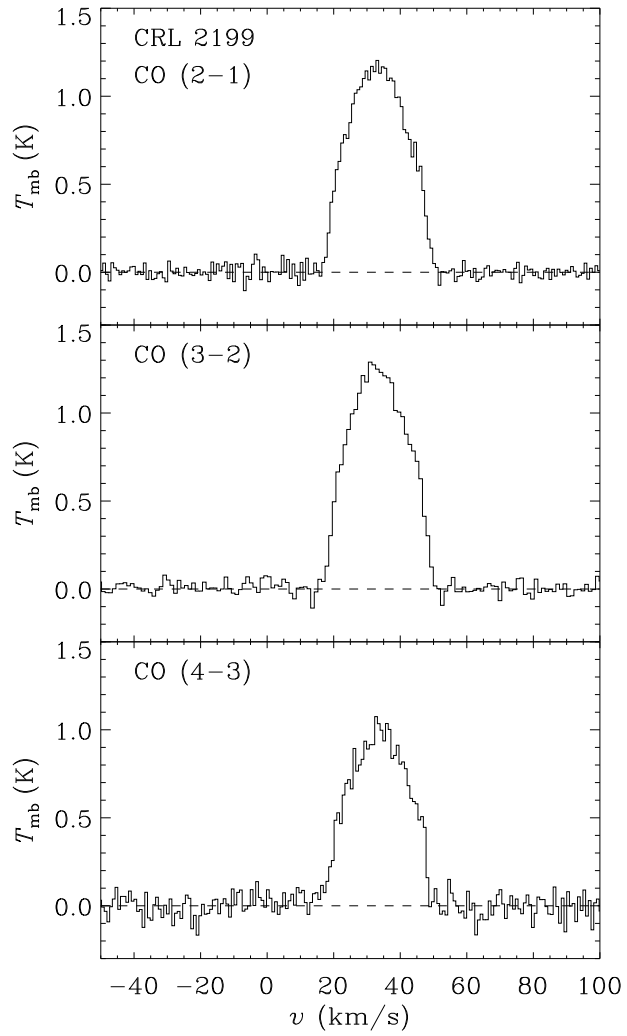


Fig. A.12. Idem – CRL 2199

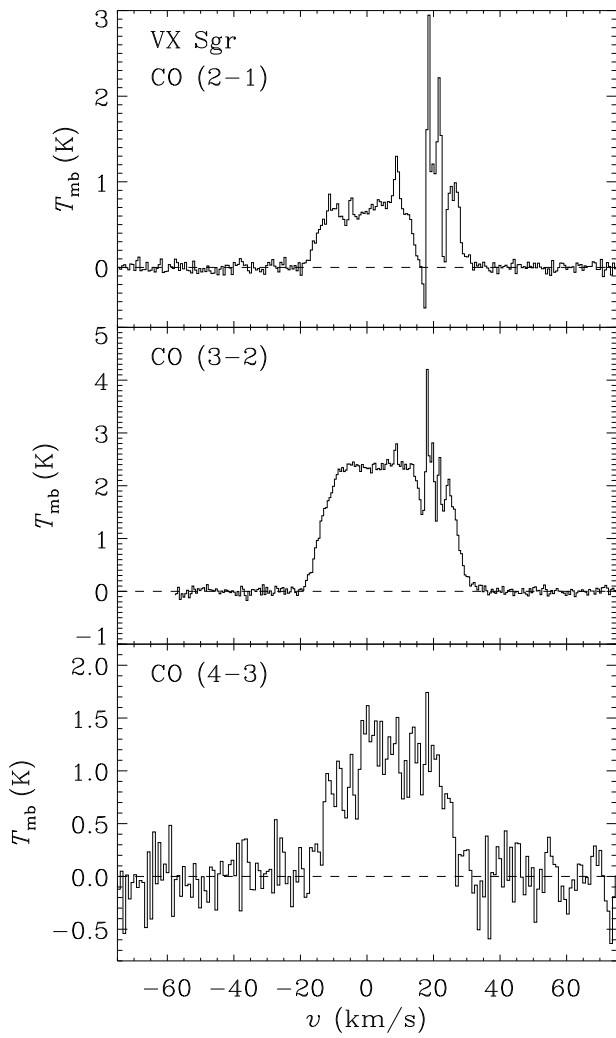


Fig. A.11. Idem – VX Sgr

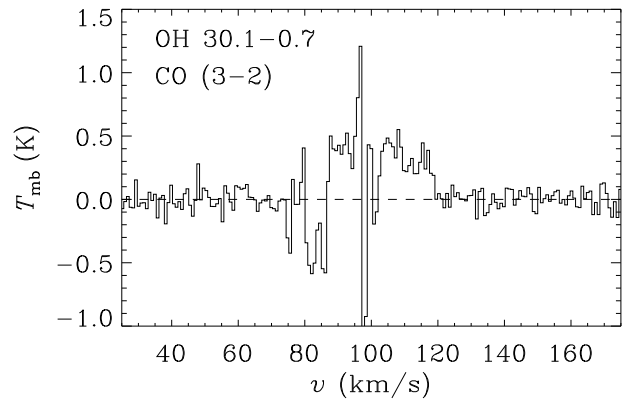


Fig. A.13. Idem – OH 30.1-0.7

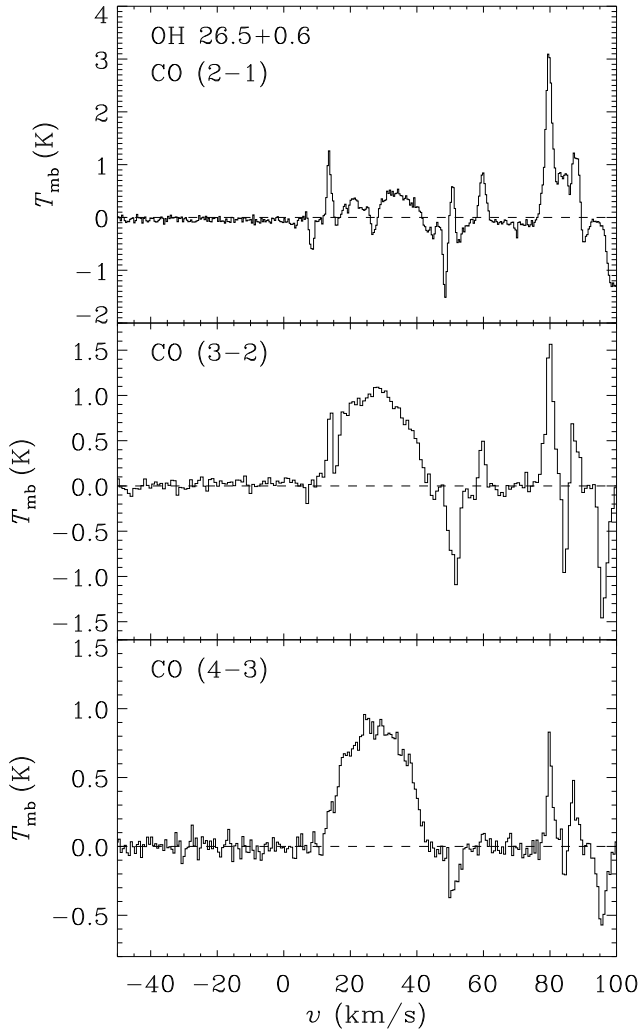


Fig. A.14. Idem – OH 26.5+0.6

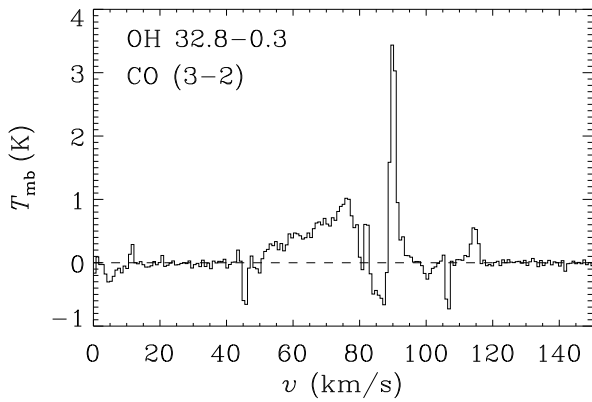


Fig. A.15. Idem – OH 32.8-0.3

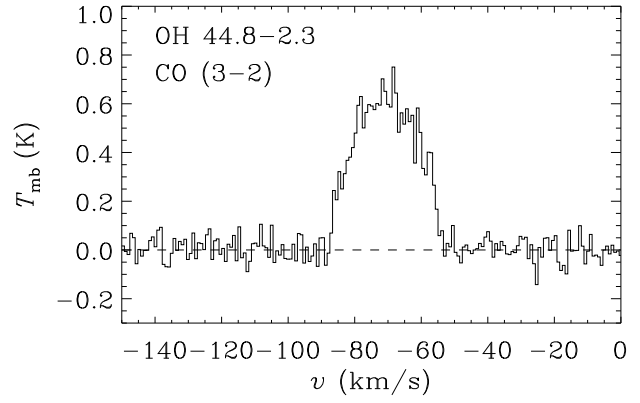


Fig. A.16. Idem – OH 44.8-2.3

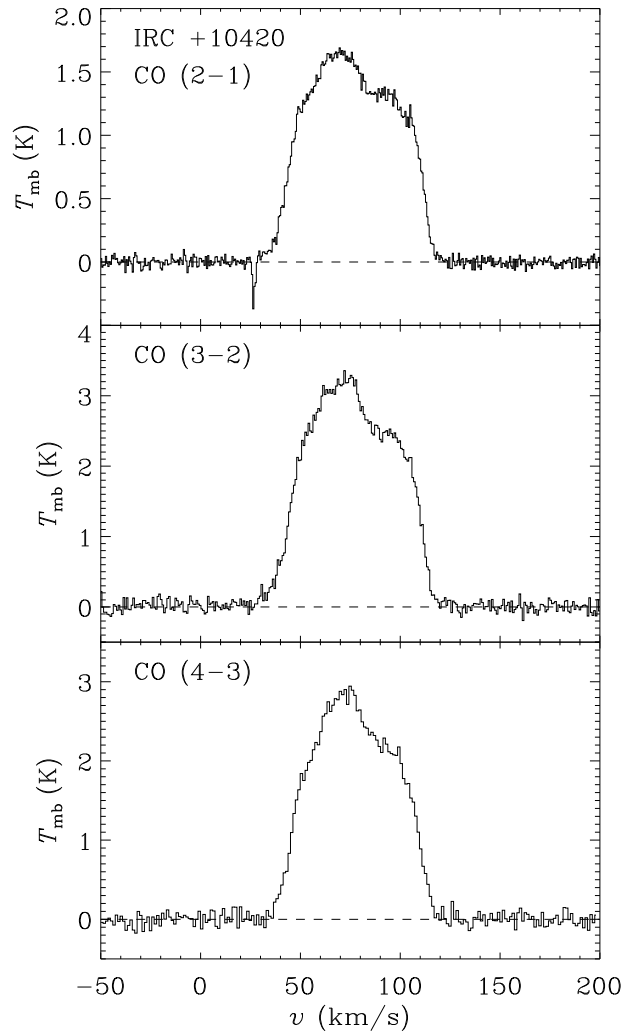


Fig. A.17. Idem – IRC +10420

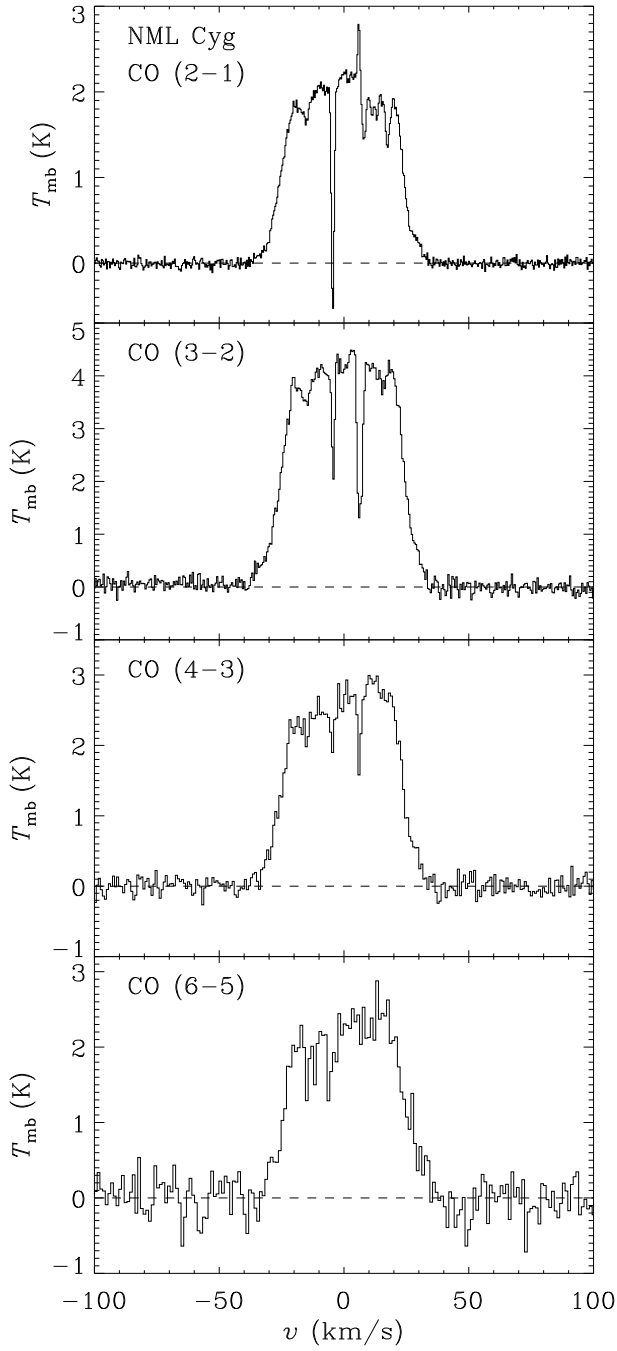


Fig. A.18. Idem – NML Cyg

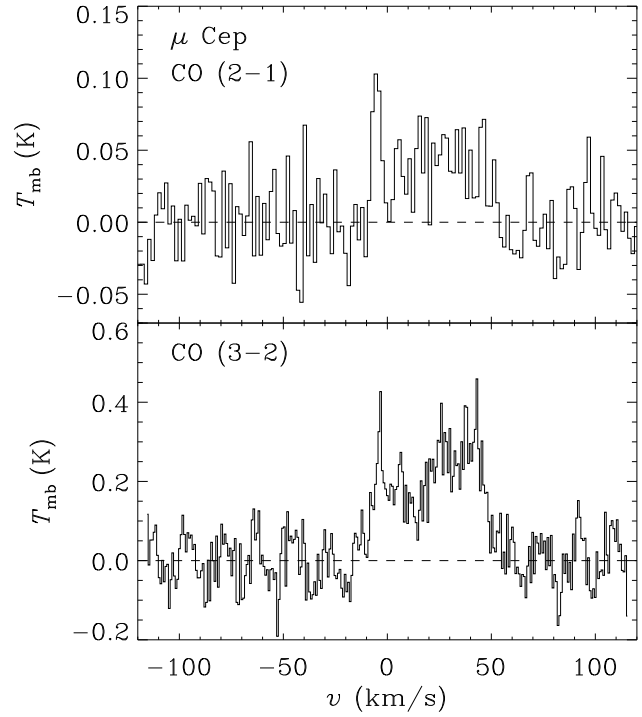


Fig. A.19. Idem – μ Cep

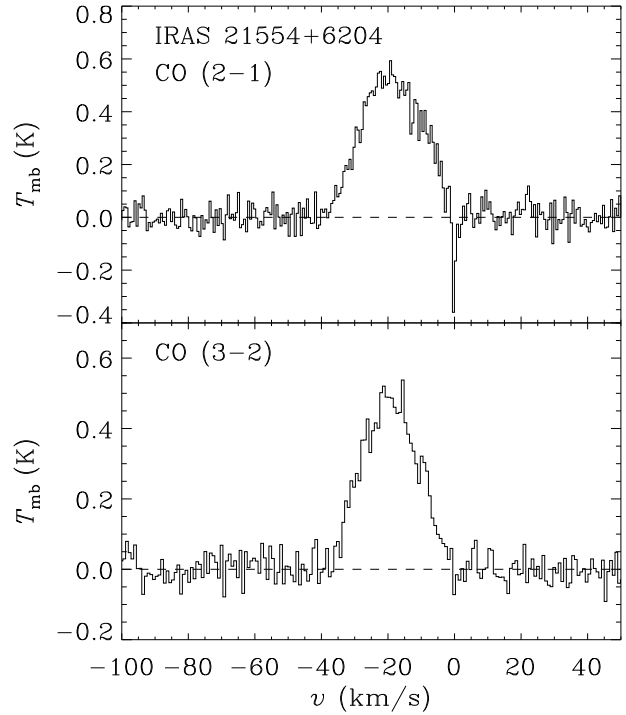


Fig. A.20. Idem – IRAS 21554+6204

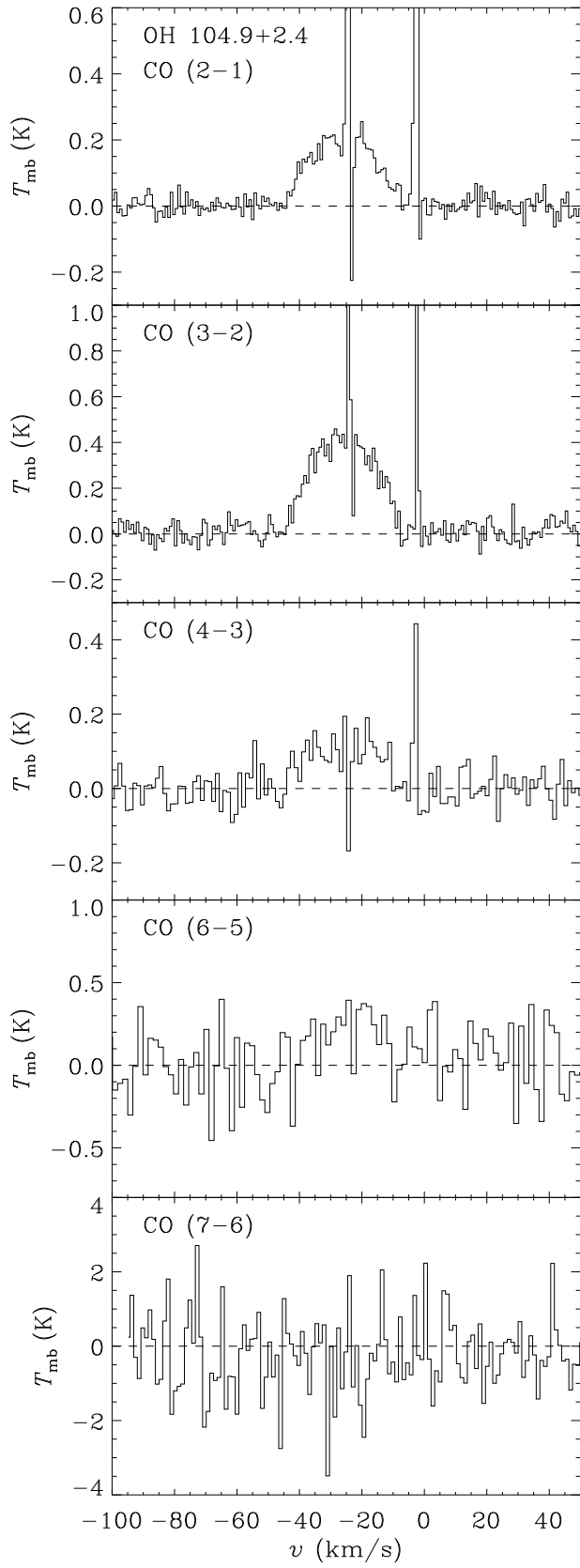


Fig. A.21. Idem – OH 104.9+2.4